Temperature and particle-size dependence of the equilibrium order parameter of FePt alloys

R. V. Chepulskii[1,2,*] and W. H. Butler[1]
[1]*Center for Materials for Information Technology, University of Alabama, Box 870209, Tuscaloosa, Alabama 35487-0209, USA*
[2]*Department of Solid State Theory, Institute for Metal Physics, N.A.S.U., Vernadsky 36, Kyiv-142, UA-03680, Ukraine*
(Received 26 April 2005; revised manuscript received 18 July 2005; published 26 October 2005)

First, second, and third nearest-neighbor pair mixing potentials for equiatomic FePt alloys were calculated from first principles by the Connolly-Williams method within the canonical cluster expansion formalism. It was demonstrated that these Connolly-Williams potentials (based on completely *ordered* states) and the corresponding Korringa-Kohn-Rostoker coherent potential approximation (KKR-CPA) potentials (based on completely *disordered* states) can be brought into very close correspondence to each other simply by increasing the magnitude of the strain-induced interactions added to the KKR-CPA potential. Using the mixing potentials obtained in this manner, the dependence of equilibrium $L1_0$ ordering on temperature was studied for bulk and for (approximately) spherical nanoparticles ranging in size from 2.5 to 6 nm. The order parameter was calculated using Monte Carlo simulations and the analytical ring approximation. The calculated order-disorder temperature for bulk (1495–1514 K) was in relatively good agreement (4% error) with the experimental value (1572 K). For nanoparticles of finite size, the (long-range) order parameter changed continuously from unity to zero with increasing temperature. Rather than a discontinuity indicative of a phase transition, we obtained an inflection point in the order as a function of temperature. This inflection point occurred at a temperature below the bulk phase transition temperature and decreased as the particle size decreased. Our calculations predict that 3.5-nm-diam particles in configurational equilibrium at 600 °C (a typical annealing temperature for promoting $L1_0$ ordering) have an $L1_0$ order parameter of approximately 0.84 (compared to a maximum possible value equal to unity). According to our investigations, the experimental absence of (relatively) high $L1_0$ order in 3.5-nm-diam nanoparticles annealed at 600 °C or below is primarily a problem of *kinetics* rather than equilibrium.

DOI: 10.1103/PhysRevB.72.134205 PACS number(s): 61.46.+w, 75.50.Tt, 64.70.Nd, 61.66.Dk

I. INTRODUCTION

Self-assembled, monodispersed FePt nanoparticles are being intensively investigated for possible future application as an ultrahigh-density magnetic storage medium. In order to be useful as a storage medium, however, these particles, because of their extremely small volume V, must have sufficiently high magnetic anisotropy K_u to withstand thermal fluctuations of the direction of magnetization. This requires values of the thermal stability factor $(K_uV)/(k_BT)$ of approximately 50. The particles are usually produced by a "hot soap" process that yields a disordered fcc solid solution alloy (e.g., Ref. 1). Such particles are not useful for information storage in the as-made state because they are paramagnetic at room temperature due to their low magnetic anisotropy.

Typically, the particles are annealed at a temperature $T \simeq 600$ °C in order to induce an ordered $L1_0$ phase.[2,3] The layered $L1_0$ phase[4] is known from studies of bulk alloys to have an extremely high magnetic anisotropy ($K_u \cong 7 \times 10^7$ erg/cm^3). This value of magnetic anisotropy would provide a sufficiently large thermal stability factor to make 3.5-nm-diam particles viable for information storage.

Unfortunately, it appears to be difficult to achieve a high degree of long-range atomic order in FePt *nanoparticles* with $\lesssim 4$ nm diameter by annealing at $T \lesssim 600$ °C (e.g., Ref. 2). One can consider two possible reasons for the fact that it has not been possible to obtain well ordered small particles. First, the observed order may be low because the particle is *not* in its equilibrium state due to the slow kinetics at low temperatures. Alternatively, the *equilibrium* order itself may be low even at relatively low temperatures because of the small size of nanoparticles. The latter explanation was suggested in Ref. 2. There, the order-disorder phase transition temperature was estimated to decrease with decrease of particle size. For particle sizes less than 1.5 nm in diameter, the phase transition temperature was found to be below the typical annealing temperature ($T \simeq 600$ °C). Therefore, particles of diameter less than 1.5 nm were predicted to have no long range order in their equilibrium state at 600 °C. This explanation is in qualitative agreement with experiment. The difference between the experimental (4 nm) and theoretical (1.5 nm) critical size for disappearance of $L1_0$ order at 600 °C was attributed to the neglect of nanoparticle surface effects.

From our point of view, however, the results obtained in Ref. 2 require verification because of the limitations of the theoretical models used in that study. Namely, the interatomic potentials in alloys usually are much more complicated and long-ranged than the nearest-neighbor Lennard-Jones model that was used. In addition, the order-disorder phase transition temperature was estimated in Ref. 2 by comparing the free energies of completely ordered and completely disordered states, whereas in reality, the ordered state approaches (with increasing temperature) the phase transition point being not completely ordered. Also, the disordered state would be expected to approach the phase transition (with decreasing temperature), not with a completely random atomic distribution, but with an atomic distribution that has substantial short-range order. Moreover, it is known[5] that

there is no formal phase transition in a finite system.

The aim of the present paper is to determine the reason for the low value observed experimentally for the $L1_0$ order parameter in small nanoparticles at typical annealing temperatures through the use of theoretical models that do not have the above-described limitations.[6]

Presently, there are two main approaches for calculating effective atomic interactions (called mixing potentials in this paper) that determine the configurational behavior of atoms in an alloy. One is the Connolly-Williams method,[7–9] which is based on a first-principles calculation of the energies of a number of completely *ordered* structures. The second approach is based on the coherent potential approximation (CPA) for the completely *disordered* state (e.g., Ref. 10). In the present paper we utilize and compare both approaches. The first-principles calculations that we performed in order to implement the Connolly-Williams method were carried out in the generalized gradient approximation to density-functional theory, using the VASP program package.[11] To obtain mixing potentials from the CPA we used data obtained within the Korringa-Kohn-Rostoker coherent potential approximation[12–15] (KKR-CPA) in Ref. 16.

To study the temperature, concentration, and size dependences of equilibrium long-range order in FePt bulk and nanoparticles we used Monte Carlo simulations (utilizing the Metropolis algorithm[17]) and the analytical ring approximation.[18] The details of the models used in our study are described below in the corresponding sections. In our opinion, the most important limitation of our model is the use in nanoparticles of potentials derived for the bulk. Some of the effects of this assumption are described in Sec. IX.

II. LATTICE GAS MODEL AND CLUSTER EXPANSION

We consider an Fe-Pt alloy in the framework of the two-component A-B lattice gas model (e.g., $A=\mathrm{Pt}, B=\mathrm{Fe}$). In this model,[19] two types of atoms are distributed over the sites of a rigid crystal lattice. The atoms are allowed to be situated only at the crystal lattice sites, and each site can be occupied by only one atom. The atoms interact through the lattice potentials and can exchange their positions according to Gibbs statistics. The lattice gas model is the most commonly used model for describing substitutional ordering in alloys (e.g., Refs. 10 and 20).

The configurational state of the lattice gas considered here can be defined by the set of configurational variables $C_{\mathbf{R}}^{\alpha}$:

$$C_{\mathbf{R}}^{\alpha} = \begin{cases} 1, & \text{if the site } \mathbf{R} \text{ is occupied by an } \alpha\text{-type atom,} \\ 0, & \text{otherwise,} \end{cases} \tag{1}$$

where $\alpha=A$, B, and $\mathbf{R}$ is the site radius vector. Because each site contains only one atom, we have

$$C_{\mathbf{R}}^{A} + C_{\mathbf{R}}^{B} = 1 \Rightarrow C_{\mathbf{R}}^{B} = 1 - C_{\mathbf{R}}^{A}. \tag{2}$$

Thus any configurational state of the two-component lattice gas model (i.e., any particular distribution of atoms over the sites) can be determined by $C_{\mathbf{R}}^{A}$ variables only.

The energy of any state can be expanded as (e.g., Sec. II in Ref. 21)

$$E = E_0 + \sum_{\alpha,\mathbf{R}} E_{\mathbf{R}}^{\alpha} C_{\mathbf{R}}^{\alpha} + \frac{1}{2} \sum_{\alpha_1,\alpha_2} \sum_{\mathbf{R}_1,\mathbf{R}_2} E_{\mathbf{R}_1,\mathbf{R}_2}^{\alpha_1,\alpha_2} C_{\mathbf{R}_1}^{\alpha_1} C_{\mathbf{R}_2}^{\alpha_2}, \tag{3}$$

where E_0, $E_{\mathbf{R}}^{\alpha}$, and $E_{\mathbf{R}_1,\mathbf{R}_2}^{\alpha_1,\alpha_2}$ are the coefficients of the energy expansion. $E_{\mathbf{R}_1,\mathbf{R}_2}^{\alpha_1,\alpha_2}$ can be considered as pair interactions between two atoms of types α_1 and α_2 situated at $\mathbf{R}_1$ and $\mathbf{R}_2$ sites, respectively. Expression (3) is usually called a cluster expansion.[22] In Eq. (3), the terms proportional to the powers of $C_{\mathbf{R}}^{\alpha}$ higher than second power are not taken into account. Terms corresponding to nonpair atomic interactions were found to be small in equiatomic FePt alloys (see the discussion in Sec. III), so we excluded them from the beginning.

By the use of Eq. (2), one can exclude $C_{\mathbf{R}}^{B}$ from Eq. (3) and get

$$E = V^{(0)} + \sum_{\mathbf{R}_1} V_{\mathbf{R}_1}^{(1)} C_{\mathbf{R}_1}^{A} + \frac{1}{2} \sum_{\mathbf{R}_1,\mathbf{R}_2} V_{\mathbf{R}_1,\mathbf{R}_2}^{(2)} C_{\mathbf{R}_1}^{A} C_{\mathbf{R}_2}^{A}, \tag{4}$$

where $V^{(i)}$ $(i=0,1,2)$ we call mixing potentials (other names are "interchange energies" and "effective cluster interactions"):

$$V_{\mathbf{R}_1}^{(1)} = E_{\mathbf{R}_1}^{A} - E_{\mathbf{R}_1}^{B} + \sum_{\mathbf{R}_2} [E_{\mathbf{R}_1,\mathbf{R}_2}^{A,B} - E_{\mathbf{R}_1,\mathbf{R}_2}^{B,B}], \tag{5}$$

$$V_{\mathbf{R}_1,\mathbf{R}_2}^{(2)} = E_{\mathbf{R}_1,\mathbf{R}_2}^{A,A} - 2E_{\mathbf{R}_1,\mathbf{R}_2}^{A,B} + E_{\mathbf{R}_1,\mathbf{R}_2}^{B,B}, \tag{6}$$

$V^{(0)}$ is the energy of lattice gas with B atoms only. The knowledge of the mixing potentials is important because they determine the energetics of the lattice gas. A number of methods have been elaborated for calculation of the mixing potentials.

III. CONNOLLY-WILLIAMS METHOD

Within the Connolly-Williams method,[7–9] the mixing potentials are assumed to have the symmetry of the disordered state—i.e., to be configurationally independent. Thus, $V_{\mathbf{R}}^{(1)}$ is independent of $\mathbf{R}$ and the pair mixing potential $V_{\mathbf{R}_1,\mathbf{R}_2}^{(2)}$ depends only on the difference $\mathbf{R}_1-\mathbf{R}_2$:

$$V_{\mathbf{R}}^{(1)} = V^{(1)}, \quad V_{\mathbf{R}_1,\mathbf{R}_2}^{(2)} = V_{\mathbf{R}_1-\mathbf{R}_2}^{(2)}. \tag{7}$$

The pair mixing potential $V_{\mathbf{R}}^{(2)}$ can be represented by its values $V_s^{(2)}$ for different coordination shells:

$$V_s^{(2)} \equiv V_{\mathbf{R}_s}^{(2)}, \tag{8}$$

where $\mathbf{R}_s$ is the radius vector connecting any given site with another site that belongs to the sth coordination shell with respect to that given site. Generally, we define a coordination shell for a given site to be all of the sites that interact with a given site with the same value of the pair mixing potential.

Within the Connolly-Williams method, the energies E_i $(i=1,2,\ldots,N_{\varepsilon})$ of some N_{ε} structures (i.e., long-range-ordered periodic atomic distributions sometimes called superstructures—for example, $L1_0$) are calculated by first-

principles methods. Writing Eq. (4) for each of those N_ε structures, one can get the following system of linear equations:

$$\begin{cases} \varepsilon_i = V^{(1)} c_i + \sum_{s=1}^{N_s} S_{is} V_s^{(2)}, \\ i = 1,2,\ldots,N_\varepsilon, \end{cases} \tag{9}$$

where

$$\varepsilon_i = \frac{E_i - V^{(0)}}{N_i^A + N_i^B}, \tag{10}$$

N_i^A and N_i^B are the total numbers of A and B atoms in the ith structure, respectively, S_{ij} are the structural coefficients, and c_i is the concentration of A atoms:

$$c_i = N_i^A/(N_i^A + N_i^B). \tag{11}$$

The energy $V^{(0)}$ of a pure B crystal is also calculated by first-principles methods. So the problem is to find N_s+1 unknown mixing potentials $V^{(1)}$ and $V_s^{(2)}$ $(s=1,2,\ldots,N_s)$ that give the best fit [through Eq. (9)] to the energies ε_i $(i=1,2,\ldots,N_\varepsilon)$ calculated by the first-principles methods.

Usually, the choice of the structures to be used is random with a predisposition towards the well-known ones that are more easily calculated. It is preferable that the structures be experimentally observable for the alloy under consideration and that they correspond to the ground state or at least a low-energy state (e.g., Refs. 7 and 8). However, since all configurations are possible for Eqs. (4) and (9), *any* convenient structure can be used for the determination of the mixing potentials.

So, in contrast to the usual procedure, our criterion for the choice of the structures is only that they be linearly independent. By *linear independence* we mean that the main determinant of the system (9)—i.e., the determinant of the matrix $\|\delta_{1,j}(c_i - S_{ij}) + S_{ij}\|$—is not zero $(i,j=1,2,\ldots,N_\varepsilon;\ \delta$ is the Kronecker delta). Among the linearly independent structures we chose those with fewer than 20 atoms per unit cell in order to reduce the cost of the first-principles calculations. Note that if all of the structures have the same composition (see below), there is only one ground state (if it is not degenerate) and the usual procedure of using only (or mainly) the ground states within the Connolly-Williams method is inapplicable. One may hypothesize that the use of nonground states should expand the applicability of the resulting mixing potentials to higher temperatures.

In the present paper we mainly (except Figs. 9 and 12) study the Fe-Pt alloy close to equiatomic composition $c=0.5$. Accordingly, we chose input structures to be of the same composition $c_i=0.5$. The reason for doing so is the following. If we use structures of different compositions to find the mixing potentials, we imply that the mixing potentials are exactly the same for all compositions. However, the electronic structure of an alloy system generally depends strongly on composition. (For example, at low temperatures the FePt alloy shows a strong dependence of magnetic properties on composition: Fe_3Pt, FePt, and $FePt_3$ are ferromagnetic, ferromagnetic, and antiferromagnetic, respectively.) The mixing potentials are mainly determined by the electronic structure of the alloy and, therefore, one may expect a compositional dependence of the mixing potentials as well. For example, such a dependence of pair mixing potential was found numerically within KKR-CPA in Ref. 23. For such systems with a strong compositional dependence of properties one may expect faster convergence of the Connolly-Williams method results with respect to increase of N_ε and N_s when the considered structures are of the same composition. Such an approach corresponds to the canonical cluster expansion formalism[24] and was applied, e.g., in Ref. 25.

Note that the Connolly-Williams method is usually applied using structures of different compositions assuming compositional independence of mixing potentials (grand canonical cluster expansion formalism[24]). In this approach, the compositional dependence of alloy properties (e.g., the asymmetry of the phase diagram with respect to $c=0.5$) manifests itself through the presence of nonpair mixing potentials.[26] In our approach the composition dependence of alloy properties arises partly from the composition dependence of the mixing potentials. This approach is similar to that used in methods based on the study of the disordered state (e.g., CPA). Therefore, a direct comparison of Connolly-Williams and CPA potentials is possible (see below Sec. V).

The first-principles calculations were performed within the generalized gradient approximation to density-functional theory, using the VASP program package with mainly default settings.[11] All calculations were spin polarized. The effect of lattice vibrations was omitted. All structures were totally relaxed including shape and volume relaxation of the unit cell as well as the individual displacements of atoms within the unit cell. The densities of k points using the Monkhorst-Pack mesh in the corresponding full Brillouin zones were chosen to be similar for all considered structures and approximately equal to $(8\times8\times8)/(2\pi/a)^3$ (a is the fcc lattice parameter), but the convergence of the results was checked to verify that it was sufficient in all cases. For the calculation of ε_i [see Eq. (10)] for *each* structure we used the quantity $V^{(0)}$ (energy of pure Fe) calculated separately using the same parameters (both unit cell and VASP parameters) as for the corresponding structure. We believe that this approach diminished the error of the *difference* $E_i - V^{(0)}$ (and correspondingly of ε_i) compared to the error of E_i and $V^{(0)}$ themselves, due to the systematic cancellation of errors.

The $L1_0$ structure was included among the structures considered. In this case, after atom position relaxation, we obtained 3.852 Å and 3.757 Å for the a and c lattice parameters of the corresponding tetragonal lattice, respectively ($c/a=0.975$). For comparison the experimental values are 3.847 Å and 3.715 Å ($c/a=0.966$).[27] In addition, our calculated results showed the $L1_0$ ferromagnetic structure to be more stable (i.e., has lower energy) than the antiferromagnetic one in accordance with experiment. We believe that this good correspondence between theoretical and experimental results confirms the adequacy of our VASP first-principles calculations.

The results of the application of our Connolly-Williams method to FePt are presented in Figs. 1–4 and Table. I. In Fig. 2, in analogy with Ref. 28, we present the dependences

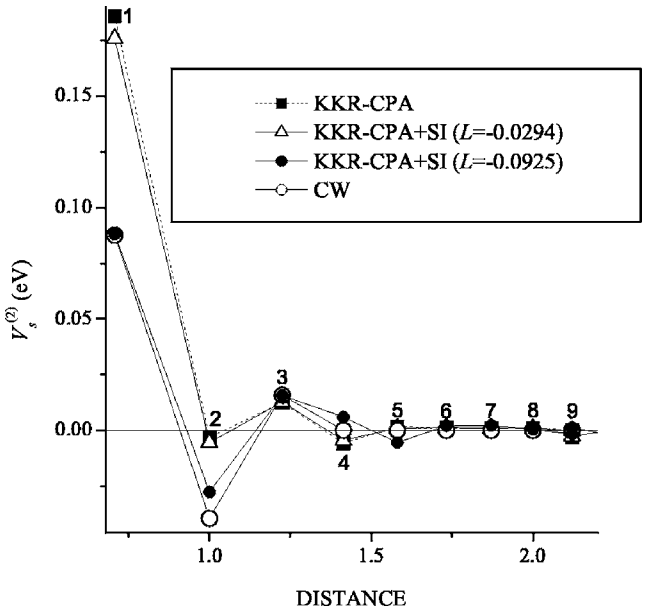

FIG. 1. The values of pair mixing potential $V_s^{(2)}$ for nine coordination shells ($s=1,2,\ldots 9$) corresponding to the KKR-CPA method (KKR-CPA) and KKR-CPA plus strain-induced interactions (KKR-CPA+SI) at $L=-0.0294,-0.0925$ (see Sec. V) as well as to the Connolly-Williams method (CW) at $N_s=3, N_\varepsilon=23$ (see Sec. III). The distance is measured in fcc lattice parameter units.

of cross-validation[8] (CV) and least-squares fitting (LSF) errors

$$(\mathrm{CV})^2 = (23)^{-1}\sum_{i=1}^{23} (\varepsilon_i^{\mathrm{VASP}} - \varepsilon_i^{\mathrm{CW}i})^2, \tag{12}$$

$$(\mathrm{LSF})^2 = (23)^{-1}\sum_{i=1}^{23} (\varepsilon_i^{\mathrm{VASP}} - \varepsilon_i^{\mathrm{CW}})^2, \tag{13}$$

as well as of the phase transition temperature on N_s. In Eqs. (12) and (13), $\varepsilon_i^{\mathrm{VASP}}$ ($i=1, 2, \ldots,23$) correspond to the values obtained within the VASP code for 23 linearly independent structures (see Appendix); $\varepsilon_i^{\mathrm{CW}}$ are obtained for those structures using the mixing potentials obtained by the Connolly-Williams method at $N_\varepsilon=23$; $\varepsilon_i^{\mathrm{CW}i}$ are obtained for those structures using the mixing potentials obtained by the Connolly-Williams method at $N_\varepsilon=22$ when ith structure is excluded from fitting. Such a CV error characterizes the predictive power of these Connolly-Williams potentials within the set of 23 structures.[8]

In Fig. 3, the convergence of the results obtained by the Connolly-Williams method at $N_s=3$ is verified with respect to an increase in the number, N_ε, of structures taken into account within the method. Up to 23 linearly independent structures (see the Appendix) were considered. Note that to achieve the rapid convergence shown in Fig. 3 it was important to begin with structures having the highest symmetries. The use of linearly independent structures guarantees that the good convergence (starting from $N_\varepsilon \simeq 8$) is not caused by a simple similarity of structures.

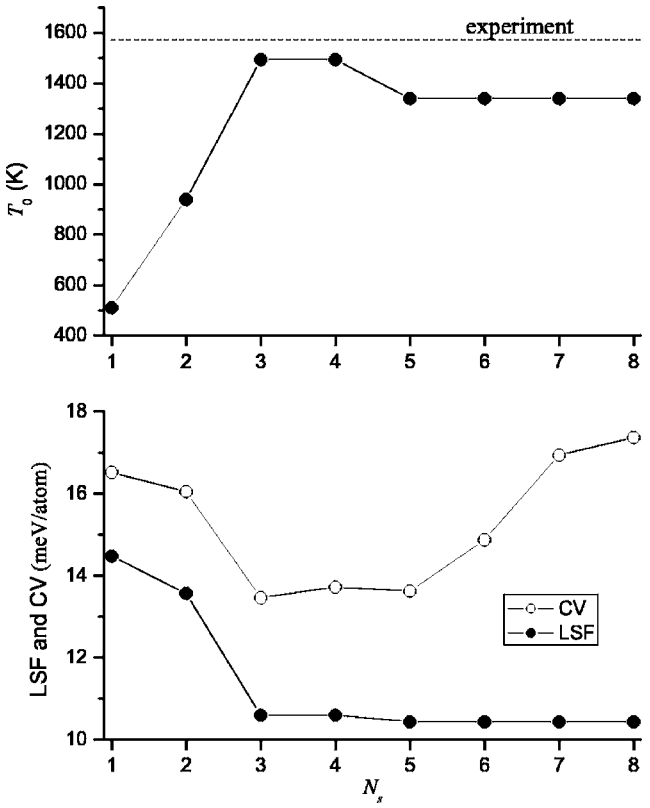

FIG. 2. The values of cross-validation (CV) and least-squares fitting (LSF) errors [see Eqs. (12) and (13)] as well as of the phase transition temperature T_0 [within the ring approximation (Ref. 18)] calculated as a function of the number of pair mixing potential values N_s taking into account within the Connolly-Williams method ($N_\varepsilon=23$). Dashed line corresponds to the experimental value (Ref. 48).

In Fig. 4 we compare the values of $\varepsilon_i - V^{(1)}c_i$ [see Eqs. (9) and (10)] for each of the 23 linearly independent structures (see the Appendix). The figure shows the values calculated both directly from first principles and by the use of the mixing potentials obtained by the Connolly-Williams method at $N_s=3, N_\varepsilon=23$. The absolute differences between those two energies characterize the accuracy of Connolly-Williams fitting in the case of each structure. An LSF error of 10.59 meV was obtained. In order to check the predictive power of these Connolly-Williams potentials outside the set of 23 structures, we also calculated the energies of 5 additional structures. This set of 5 structures includes all distinguishable (but not identical to the previous 23 ones) equiatomic structures based on two-cubic unit cells in the fcc crystal lattice (see the Appendix). The LSF errors of the Connolly-Williams potential for the 5 additional structures and for all 28 structures were obtained to be 12.51 meV and 10.96 meV, respectively. It is important that if we calculate the Connolly-Williams potentials using all 28 structures ($N_\varepsilon=28$) we obtain almost the same LSF errors of the energy fitting for the first 23, last 5 and all 28 structures: 10.89 meV, 12.27 meV, and 11.15 meV, respectively. Thus, one may conclude that the comparatively lower accuracy of fitting for the last 5 structures is not caused by not including them into the fitting set. Such a high predictive power confirms our choice of using only linearly

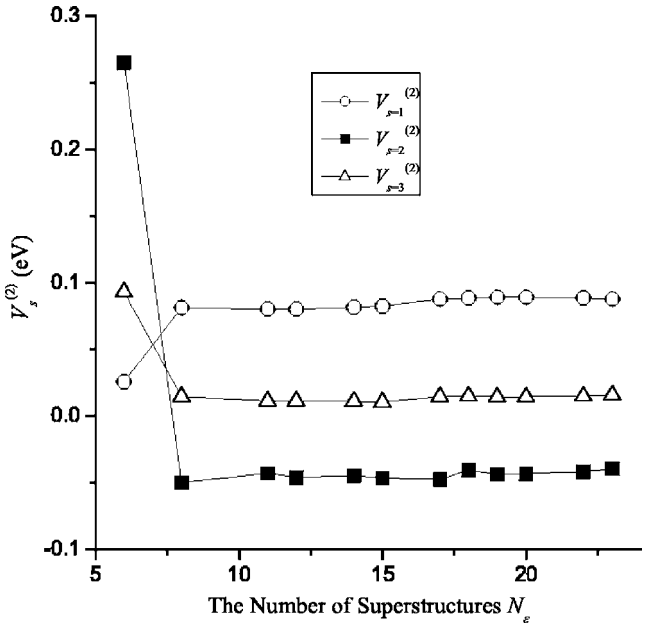

FIG. 3. The values of pair mixing potential $V_s^{(2)}$ for three coordination shells ($s=1,2,3$) obtained by the Connolly-Williams method at fixed $N_s=3$ but for different numbers N_ε of structures (all of equiatomic composition $c=0.5$) taken into account within the method.

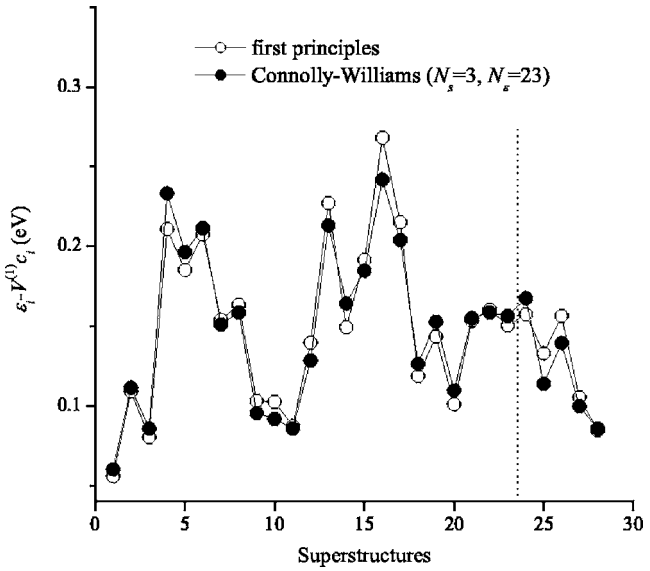

FIG. 4. The values of $\varepsilon_i - V^{(1)} c_i$ [see Eqs. (9) and (10)] for 28 equiatomic ($c_i=0.5$) structures calculated both directly from first principles and by the use of the mixing potentials obtained by the Connolly-Williams method (at $N_s=3, N_\varepsilon=23$). The differences between those two energies characterize the accuracy of Connolly-Williams fitting in the case of each structure. The first 23 structures (see the Appendix) are linearly independent and they (and only they) were used in the Connolly-Williams method. The last 5 structures (right side of the vertical dashed line) correspond to all distinguishable (but not identical to the previous 23 ones) equiatomic structures based on two-cubic unit cells in the fcc crystal lattice (see the Appendix). Those 5 structures were not used in the Connolly-Williams fitting, but they were considered in order to assess the predictive power of the obtained Connolly-Williams potentials.

independent (see above) structures in the Connolly-Williams method, because the last 5 structures in Fig. 4 are linearly dependent (but not identical) to the first 23 structures. One may suppose that the use of additional linearly dependent structures in the Connolly-Williams method would simply impose extra weight factors for some of the initial structures.

The good convergence as a function of N_ε shown in Fig. 3, the high predictive power within and outside the set of 23 structures, the small CV and LSF errors of the Connolly-Williams fitting shown in Figs. 2–4, and the position of the local minimum[29] of CV error as a function of the number of fitting parameters in Fig. 2 suggest that the neglect of nonpair mixing potentials and of pair mixing potentials outside three coordination shells (i.e., $N_s=3$) (Ref. 30) as well as consideration of $N_\varepsilon=23$ linearly independent structures is sufficient to obtain adequate results within the Connolly-Williams method for the case considered here. The small difference between the experimental bulk order-disorder phase transition temperature and that obtained using these mixing potentials[31,32] (see Fig. 2 and below Table III in Sec. VII) provides *indirect* evidence of adequacy of the potentials for equiatomic Fe-Pt. *Direct* evidence is provided by the study of the cross-validation error (Fig. 2), least-squares fitting error (Figs. 2 and 4), and the convergence achieved in Fig. 3. In Fig. 1 and Table I the pair mixing potential values obtained by the Connolly-Williams method at $N_s=3, N_\varepsilon=23$ (four fitting parameters) are shown. Uniform weight factors were used in the fitting. We obtained also $V^{(1)}=1.394$ eV.

Independent calculations within the KKR-CPA and the lattice-statics method also suggest that the atomic interaction tail outside the fourth coordination shell is weak (see below Sec. V), despite the "$k\to 0$ nonanalyticity"[7,33,34] of the Fourier transform of the corresponding pair mixing potential.

In Ref. 35, the Connolly-Williams method with structures of different concentrations was applied to FePt. Consideration was not limited to the ground-state structures. One "hypothetical" phase $L1_1$ was considered. The interchange model was restricted to two coordination shells of atomic pair interactions neglecting nonpair interactions. Only six structures were considered, making the number of unknown potential parameters equal to the number of input parameters (energies of structures). The convergence of the results obtained by the Connolly-Williams method with respect to an increase in number of considered structures was not checked. Consideration of Fig. 3 indicates that for such a small number of structures convergence may not be achieved because of errors in the energy calculation. For all structures, the relaxation of the unit cell volume was performed in a way that neglected possible unit cell shape relaxation (resulting, e.g., in its tetragonality) as well as neglecting the individual displacements of atoms within the unit cell. Using potentials calculated in this way, the phase transition temperature for equiatomic FePt bulk alloy was found to be 2070 K, which is much higher than the experimental one $\sim$1573 K.

In Ref. 36, the ratio $V_2^{(2)}/V_1^{(2)}=-0.729$ was derived through the use of first-principles calculations. This is different from the value $V_2^{(2)}/V_1^{(2)}=-0.45$ obtained by the Connolly-Williams method used in the present paper. It is

TABLE I. The values of pair mixing potential $V_s^{(2)}$ for 17 coordination shells ($s=1,2,\ldots,17$) corresponding to the KKR-CPA method (KKR-CPA), strain-induced interactions (SI) at $L=-0.0294$, and KKR-CPA method plus strain-induced interactions at $L=-0.0294$ (KKR-CPA+SI) (see Sec. V) as well as calculated by the (CW) Connolly-Williams method at $N_s=3, N_\varepsilon=23$ (see Sec. III). See also Fig. 1. The Cartesian coordinates of vector **R** are given in $a/2$ units, where a is the fcc lattice parameter. Potential values are in meV units.

Shell	**R**	$\lvert\mathbf{R}\rvert/a$	KKR-CPA	SI	KKR-CPA+SI	CW
1	110	0.707	185.855	−9.879	175.976	87.69
2	200	1.000	−2.997	−2.484	−5.481	−39.46
3	211	1.225	12.413	0.326	12.739	15.85
4	220	1.414	−5.714	1.173	−4.541	
5	310	1.581	1.727	−0.724	1.003	
6	222	1.732	1.214	0.091	1.304	
7	321	1.871	0.907	0.133	1.040	
8	400	2.000	0.974	−0.053	0.921	
9	411	2.121	0.147	−0.188	−0.041	
	330		−2.997	0.438	−2.560	
10	420	2.236	−0.050	−0.209	−0.258	
11	332	2.345	0.015	0.030	0.045	
12	422	2.449	0.099	0.060	0.160	
13	431	2.550	−0.075	0.074	−0.001	
	510		0.030	−0.058	−0.028	
14	521	2.739	−0.006	−0.073	−0.079	
15	440	2.828	−0.042	0.163	0.121	
16	433	2.915	0.008	0.019	0.027	
	530		−0.008	−0.058	−0.066	
17	442	3.000	−0.007	0.023	0.016	
	600		0.000	−0.037	−0.037	

difficult to determine the reason for this difference because details of the first-principles calculations of Ref. 36 are not reported. It is possible that the elastic contribution to the mixing potential neglected in Ref. 36 is responsible for the difference. In Ref. 36 the value of $V_1^{(2)}=96$ meV (in our designation) was fit by reproducing the experimental bulk phase transition temperature. This implies a value of the quantity $V_2^{(2)}$ of=−70 meV. For comparison, our Connolly-Williams potential values (see Table I) are very similar for the first coordination shell but almost a factor of 2 smaller for the second one. In addition, for the third shell, the Connolly-Williams potential is nonzero. Of course, the experimental bulk phase transition temperature is not reproduced perfectly by our set of Connolly-Williams mixing potentials which was obtained without fitting to experiment data (see Table III below in Sec. VII).

IV. $L1_0$ PARALLEL ANTIPHASE DOMAINS

For the case of the $L1_0$ structure, there is a possibility of creating parallel antiphase domains—i.e., the regions where the same $L1_0$ structures are shifted with respect to one another by the distance $a/2$ along the z axis perpendicular to the $L1_0$ layers. The antiphase domains are usually created as a result of the nucleation and growth of the $L1_0$ structure in different places as the initially disordered sample is cooled below the order-disorder phase transition temperature. The antiphase boundaries (APB's) between the antiphase domains contribute to the total energy, making the existence of antiphase domains favorable or unfavorable depending on the sign of the antiphase boundary energy.

TABLE II. The energies δE_a and δE_{2a} of parallel APBs in the $L1_0$ structure in the cases of a and $2a$ distance between parallel APBs, respectively. The values shown are per two atoms in one APB (in eV units) and were calculated by first principles using the VASP program package (Ref. 11). In the relaxed case, we minimized the total energy with respect to the variation of the size and shape of the unit cell as well as the local displacements of atoms within the unit cell. In the unrelaxed case, the atoms were assumed to occupy the sites of a rigid fcc lattice with the lattice parameters assumed to be the same as in the relaxed case, neglecting all the local displacements of atoms within the unit cell.

	Unrelaxed	Relaxed
δE_a	0.223	0.213
δE_{2a}	0.213	0.198
$\delta E_a-\delta E_{2a}$	9.80×10^{-3}	1.59×10^{-2}

It is easy to show that such parallel APB energies vanish in the case of only nearest-neighbor interactions. Thus, first-principles calculation of parallel APB energies is important because it allows one to test the adequacy of the nearest-neighbor interaction model for FePt. In addition, knowledge of the parallel APB energy is helpful for interpretation of Monte Carlo simulation results (see below Sec. VI) for the order parameter obtained by averaging in real space.

In order to estimate the parallel APB energies, we calculated the values of E_0, E_a, and E_{2a}—i.e., the total energies of the pure $L1_0$ structure and of two structures composed of antiphase domains periodically repeated along the y direction with steps a and $2a$, respectively (corresponding to the structures 1–3 in Appendix). The differences δE_a and δE_{2a},

$$\delta E_a = E_a - E_0, \quad \delta E_{2a} = E_{2a} - E_0, \tag{14}$$

can be considered as the total energies of a parallel APB in the corresponding two cases. The results of the calculations are presented in Table. II. Note that, besides the energies of the parallel APB's themselves, δE_a and δE_{2a} also contain some contribution from the interaction between parallel APB's. Such a contribution must decrease with increasing distance between parallel APB's. The small difference between δE_a and δE_{2a} (see Table II) indicates that the interaction between parallel APB's in the two cases considered is small and short ranged. It is somewhat larger in the relaxed case in accordance with the longer range of elastic interactions. The positiveness of δE_a and δE_{2a} indicates that parallel APB's are not energetically favorable. The nonzero values of δE_a and δE_{2a} mean that the nearest-neighbor interaction

TABLE III. The values of *bulk* order-disorder phase transition temperature measured experimentally (Experiment) (Ref. 48) and obtained by the use of mixing potentials $V_s^{(2)}$ corresponding to the KKR-CPA method (KKR-CPA), KKR-CPA method plus strain-induced interactions at $L=-0.0294, -0.0925$ (KKR-CPA+SI), and Connolly-Williams method (CW); see Table. I. The theoretical values were calculated within the ring approximation (ring) and by Monte Carlo simulations (MC).

$V_s^{(2)}$	T_0 (K)
Experiment	1572
CW	1495 (ring), 1514 (MC)
KKR-CPA	1610 (ring)
KKR-CPA+SI ($L=-0.0294$)	1552 (ring)
KKR-CPA+SI ($L=-0.0925$)	997 (ring)

model is not adequate for a description of FePt alloy in accordance with results obtained in Sec. III.

V. KKR-CPA AND STRAIN-INDUCED INTERACTIONS

Elsewhere,[14,15] detailed procedures have been described for calculating effective atomic interactions (pair mixing potentials) within the KKR-CPA methodology.[12,13] KKR-CPA-based effective atomic interactions are determined from the response of the electronic structure of the high-temperature, disordered alloy to small-amplitude concentration waves. The results obtained within KKR-CPA in Ref. 16 in the case of $Fe_{0.5}Pt_{0.5}$ paramagnetic[37] alloy are presented in Fig. 1 and Table. I.

From Fig. 1 and Table I one may conclude that the Connolly-Williams and KKR-CPA potentials (both corresponding to equiatomic concentration $c=0.5$) are similar but not identical. In both, only the three first coordination shells are substantially different from zero. The signs of the potential values for the first three coordination shells are the same within both methods. However, the absolute value of the Connolly-Williams potential for the first coordination shell is considerably smaller than that of the KKR-CPA. For the second shell, the situation is opposite. One may attribute the difference between the Connolly-Williams and KKR-CPA potentials to the different structural and magnetic states used for the calculations: completely ordered ferromagnetic for the former and completely disordered paramagnetic for the latter.

For verification of the correspondence of both potentials to the real FePt alloy we calculated the bulk order-disorder phase transition temperature (within the ring approximation and by a Monte Carlo simulation) using both of the calculated mixing potentials. Then we compared the obtained values with the corresponding experimental one. The results are presented in Table III. One can see that Connolly-Williams and KKR-CPA potentials underestimate and overestimate the experimental phase transition temperature, respectively, by almost the same difference.

Within the KKR-CPA calculation, the nuclei were constrained to occupy ideal fcc crystal lattice positions so the effect of inhomogeneous static atomic displacements is neglected. (The *homogeneous* ones are taken into account by minimizing the alloy's total energy with respect to the lattice parameter of the underlying lattice.) The inhomogeneous static atomic displacements are expected to be small for FePt alloy because of the small tetragonality obtained experimentally[27] and theoretically (see, e.g., above Sec. III). For verification, we calculated the corresponding strain-induced contribution to the pair mixing potential independently within the Khachaturyan[33] semiphenomenological theory based on the microscopic Matsubara-Kanzaki-Krivoglaz[34,38,39] lattice-statics method. This approach allows us to take into account the anisotropy and discrete (atomic) structure of a crystal lattice in contrast with the macroscopic continuum theory of elasticity.

To calculate the strain-induced interactions, we used the expression derived in Ref. 40 for the Fourier transform of the dynamical matrix. Platinum and iron were chosen as solvent and solute, respectively. The pair mixing potential is independent of this choice since it is symmetrical with respect to interchange of A and B; see Eq. (6). For the calculations, we used the following numerical values: the mass of a Pt atom $M=32.40\times10^{-26}$ kg; the lattice parameter $a_0=3.92$ Å; phonon frequencies, longitudinal $\omega_L=2\pi\times5.80$ and transverse $\omega_T=2\pi\times3.84$ (all in Trad s^{-1});[41] elastic constants of Pt, $C_{11}=3.580, C_{12}=2.536, C_{44}=0.774$ (all in 10^{12} dyn/cm^2).[42] The coefficient L of linear dependence of alloy lattice parameter a on the Fe concentration c,

$$a=a_0(1+Lc), \quad L=\left.\frac{1}{a_0}\frac{\partial a}{\partial c}\right|_{c=0}, \tag{15}$$

was calculated as $L=-0.0294$.[43] The concentration interval used for the calculation of L was chosen so that the Vegard rule is well fulfilled since it is a necessary condition of applicability of the Matsubara-Kanzaki-Krivoglaz lattice-statics method.[33,34,38,39]

The corresponding results for the strain-induced interactions are presented in Fig. 1 and Table. I. From them it follows that the strain-induced contribution to the pair mixing potentials is comparatively small as we expected. The addition of this contribution to the KKR-CPA potential decreases the corresponding phase transition temperature so that it is very close to the experimental one (see Table III).

From Fig. 1 and Table I one can also see that the addition of the strain-induced contribution to the KKR-CPA pair mixing potential moves it toward the Connolly-Williams potential values. To emphasize this effect, we increased the absolute value of the coefficient L from 0.0294 to 0.0925 (thus artificially increasing the strain-induced interactions) in order to bring the KKR-CPA plus strain-induced potential as close to the Connolly-Williams one as possible. The same tendency is observed in the Fourier transforms of the corresponding pair mixing potentials (see Fig. 5). One may conclude that the mixing potential calculated for the disordered state (KKR-CPA) can be brought into close agreement with the mixing potential based on the completely ordered states (Connolly-Williams method) simply by increasing the magnitude of the strain-induced interactions (which is proportional to L^2). Perhaps such an increase of the strain-induced

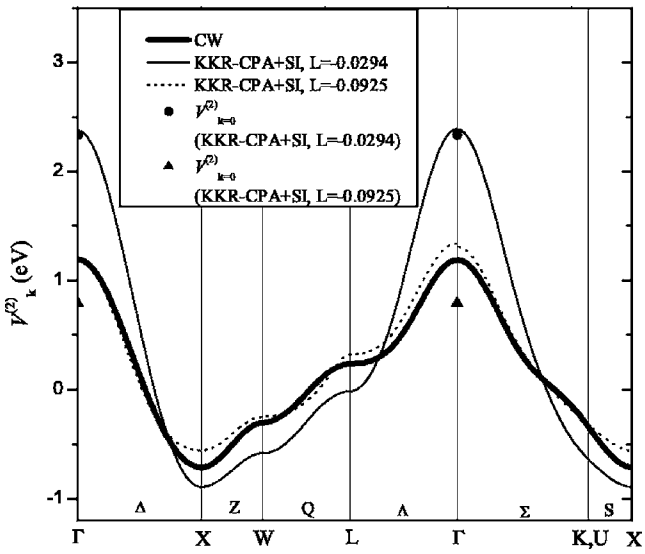

FIG. 5. The dependences of the Fourier transform $V^{(2)}_{\mathbf{k}} = \Sigma_{\mathbf{R}} V^{(2)}_{\mathbf{R}} \exp(i\mathbf{k}\cdot\mathbf{R})$ of pair mixing potential $V^{(2)}_{\mathbf{R}}$ on the wave vector along the high-symmetry directions (Ref. 44) within the corresponding first Brillouin zone. The three cases correspond to (1) the pair mixing potentials obtained by the Connolly-Williams (CW) method at $N_s=3, N_\varepsilon=23$ (see Sec. III) as well as obtained within the KKR-CPA plus strain-induced interactions (KKR-CPA+SI) at $L=-0.0294$ and $L=-0.0925$ (see Sec. V). The big bold point and triangle correspond to $V^{(2)}_{\mathbf{k}=0}$ in two cases of taking into account the strain-induced interactions, when the Fourier transform demonstrates nonanalyticity (Refs. 33, 34, 38, and 39).

interactions roughly describes the dependence of mixing potential on the order parameter (configurational excitations of the electronic structure[25,45]). It should be noticed that in other alloys for which a difference between paramagnetic and ferromagnetic potentials is large (such as $Co_{0.25}Pt_{0.75}$—see Ref. 37, one may expect that bringing the Connolly-Williams and KKR-CPA potentials into close agreement will be problematic.

Note from Table III that the phase transition temperature corresponding to the KKR-CPA potential plus the artificially increased strain-induced interactions is much lower than the experimental one. This may be explained by the roughness of our approach. Namely, by bringing the KKR-CPA $V^{(2)}_{\mathbf{k}}$ to the Connolly-Williams one in the vicinity of G point (where the difference between them is largest), we may cause too large an error in $V^{(2)}_{\mathbf{k}}$ in the vicinity of the X point, which is mainly responsible for the phase transition because of minimum of $V^{(2)}_{\mathbf{k}}$ there (see Fig. 5).[46]

From Fig. 1 and Table I it follows that the strain-induced potential is of short range despite the "$k\rightarrow 0$ nonanalyticity"[7,33,34] of its Fourier transform. One may consider this fact as an additional proof of correctness of our application of the Connolly-Williams method in Sec. III using the short-range pair mixing potential.

Below, in our Monte Carlo simulation of finite small systems, we exclusively used mixing potentials obtained by the Connolly-Williams method. We did so because the most interesting temperature region (for the aim of the present paper) corresponds to the highly ordered (both chemically and magnetically) state ($T<600$ °C). For this reason, we expect that the Connolly-Williams potentials which are based on the completely ordered states should work better in that region than the KKR-CPA potentials which are based on the completely disordered state. It is true, however, that the upper part of the temperature range of interest to us is somewhat above the Curie temperature (710 K). In this part both the Connolly-Williams and KKR-CPA approaches are problematic overestimating and underestimating short-range magnetic order, respectively. In addition, the KKR-CPA has issues related to the atomic sphere approximation and its treatment of strains.

In Ref. 47 the values of pair mixing potentials for the FePt bulk alloy were obtained within the tight binding linear orbital method. For $c=0.5$, the values for the second- and fourth-coordination-shell mixing potentials are close to the corresponding KKR-CPA ones from Ref. 16 but they are approximately a factor of 2 smaller for the first and third shells. Order-disorder transition temperatures of 662, 816, and 435 K were obtained by us for $c=0.25$, $c=0.50$, and $c=0.75$, respectively, using these potentials within the ring approximation.[18] These transition temperatures are much lower than the experimental ones (1087, 1572, and 1622 K, respectively).[48] The corresponding transition temperatures calculated in Ref. 47 are not so different from the experimental ones because the mean-field approximation, which usually overestimates the transition temperature,[20] was used. The magnitude of the discrepancy with experiment was underestimated also because an old value for the transition temperature at $c=0.75$ from Ref. 49 was used for comparison.

VI. MONTE CARLO SIMULATION

For the Monte Carlo simulations we utilized the standard Metropolis algorithm.[17] We applied free and periodic boundary conditions for the cases of spherical nanoparticles[50] and parallelepipeds, respectively.

To obtain a rapid approach to the *equilibrium* state, which is the subject of this paper, the starting configuration for each temperature was chosen to be the completely ordered one. We also used simplified kinetics in our Monte Carlo simulation. Namely, we allowed *any* two randomly chosen atoms (not only nearest neighbors) to exchange their positions *without* an additional diffusion barrier.

The absence of a monotonic change of mean values of all quantities being calculated in the Monte Carlo simulation was chosen as a criterion for the achievement of an equilibrium state. To fulfill such a criterion, it was generally necessary to perform 1000–20 000 Monte Carlo steps (i.e., the interchange of two atoms chosen at random) per site. After the equilibrium state was achieved, each calculated quantity was averaged for subsequent Monte Carlo steps. When the oscillation amplitudes of such averages (considered as a function of the number of Monte Carlo steps performed) became less than 5% (of the absolute value of the corresponding average) during the last 10% of steps (from the total number of steps carried out at an equilibrium state), the values of the averages calculated at the last Monte Carlo step were accepted as equilibrium ones.

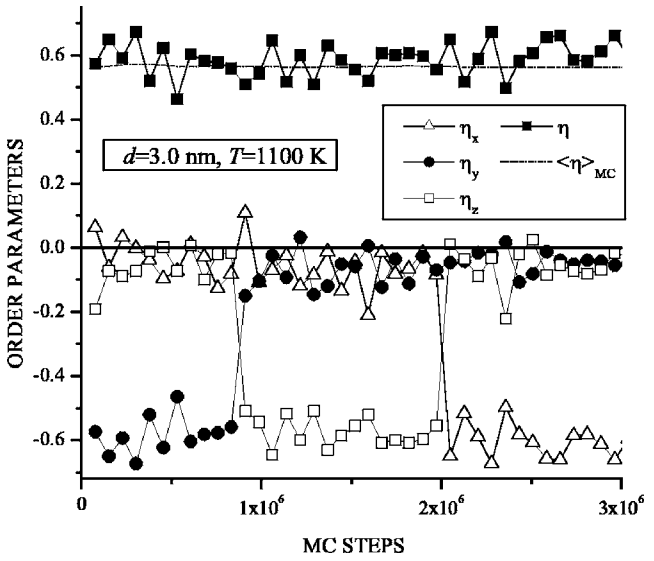

FIG. 6. The dependence of the FePt $L1_0$ order parameters on Monte Carlo steps during averaging in the equilibrium state during simulation of a spherical nanoparticle with diameter $d=3.0$ nm (see Table IV) at temperature $T=1100$ K. η_x, η_y, and η_z are the "directional" order parameters (see text): η is defined in Eq. (16).

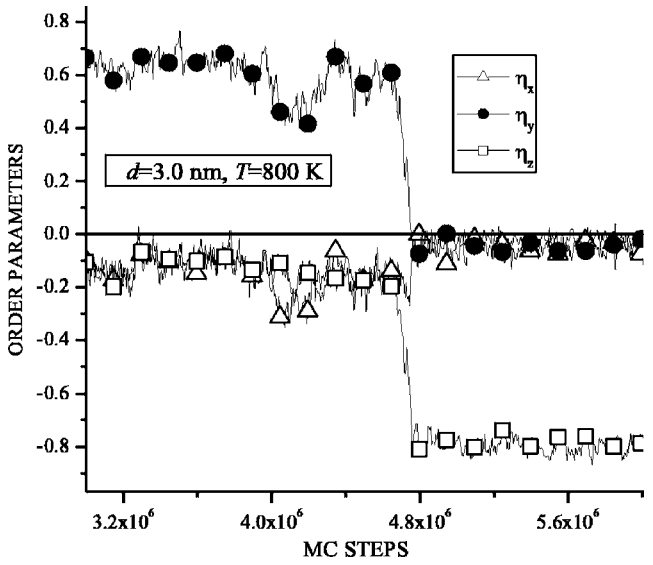

FIG. 7. The same as in Fig. 6 but for the "directional" order parameters as the spherical nanoparticle with diameter $d=3.0$ nm (see Table IV) approaches its equilibrium state at temperature $T=800$ K.

We define the equilibrium $L1_0$ order parameter $\bar{\eta}$ as the statistical average of the maximum value among three absolute values of "directional" order parameters η_x, η_y, and η_z:

$$\bar{\eta} = \langle \eta \rangle_{\mathrm{MC}}, \quad \eta = \max\{|\eta_x|, |\eta_y|, |\eta_z|\}, \tag{16}$$

where η_i $(i=x,y,z)$ is defined as the difference between the Fe atom concentrations at odd and even crystal planes perpendicular to the ith direction and $\langle \cdots \rangle_{\mathrm{MC}}$ is the statistical average over the Monte Carlo steps. We chose this definition of η because of the equivalence by symmetry of the x, y, and z directions of $L1_0$ order. In addition, one can obtain an equivalent structure (at $c=0.5$) by changing the sign of η_i, which results in the exchange of Fe and Pt atoms producing a configuration that is equivalent by symmetry to the original one. During Monte Carlo simulations, we observed fluctuations that cause transformations between these equivalent states (i.e., fluctuations in the sign and direction of η; see Figs. 6 and 7). This is in addition to the usual statistical fluctuations within one such state. The $L1_0$ order parameter $\bar{\eta}$, defined in Eq. (16) takes into account the fluctuation-induced transformations between the equivalent states. Note that because of the above-discussed symmetry equivalence, we obtain $\langle \eta_i \rangle_{\mathrm{MC}}=0$ for any $i=x,y,z$ at *any* temperature, when the statistical average is taken over a sufficiently large number of Monte Carlo steps. Note that in Ref. 36 an order parameter similar to Eq. (16) was introduced for the same reasons.

Usually during Monte Carlo simulation we observed one of the "directional" order parameters to be much larger than other two (see, e.g., Figs. 6 and 7). This means that the presence of perpendicular antiphase domains is not favorable. Examination of the atomic arrangements within the Monte Carlo simulation showed no evidence of parallel antiphase boundaries such as those discussed in Sec. IV. The absence of antiphase domains confirms the validity of our definition of the equilibrium $L1_0$ order parameter in Eq. (16).

Note that even with our simplified kinetics (see above Sec. VI), we observed a slowing down problem in approaching the equilibrium ordered state at low temperatures. For example, in Fig. 7 one can see that, for a long time, the nanoparticle can be in a metastable state with order parameter ($\sim$0.6) lower than that ($\sim$0.8) in the equilibrium state.

VII. BULK PHASE TRANSITION

To obtain an additional verification of the calculated values of mixing potential, we calculated the order-disorder phase transition temperature in the *bulk* FePt equiatomic alloy using these values. To do so, we calculated the temperature dependence of the FePt equilibrium $L1_0$ order parameter within the analytical ring approximation[18] for bulk as well as by Monte Carlo simulations for parallelepiped samples containing $N=20^3$, 40^3, and 60^3 atoms and for spherical nanoparticles with 6.0 nm diameter at (or near) equiatomic composition $c=0.5$. The results are presented in Fig. 8.

From Fig. 8 one may conclude the following. The ring approximation (which exactly corresponds to bulk—i.e., to an infinite sample) clearly shows a phase transition temperature at which the order parameter $\bar{\eta}$ drops to zero. Strictly speaking, in all the cases considered here of finite size samples (sphere and parallelepipeds) there is no phase transition in accordance with a general theorem.[5] The order parameter $\bar{\eta}$ continuously changes from unity to zero with increasing temperature, and instead of a phase transition we obtain an inflection point in the $\bar{\eta}(T)$ curve. In the case of the parallelepiped with $60^3=216\,000$ atoms, the inflection point is very similar to the phase transition. Comparing the three curves for parallelepipeds of different sizes one can imagine that the inflection point transforms into a phase transition in

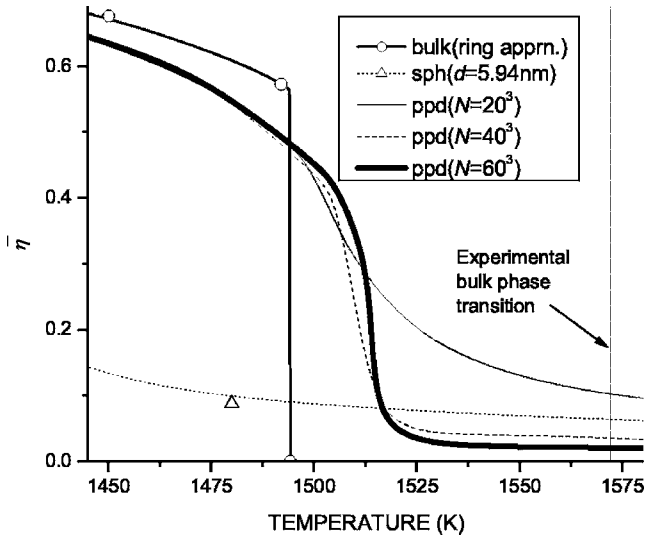

FIG. 8. The temperature dependence of the FePt equilibrium $L1_0$ order parameter $\bar{\eta}$ obtained within the analytical ring approximation (Ref. 18) for bulk ("bulk") as well as by Monte Carlo simulations for parallelepiped ("ppd") samples containing $N=20^3$, 40^3, and 60^3 atoms and the spherical ("sph") nanoparticle with $d=5.94$ nm diameter (see Table IV) at (or near) equiatomic concentration $c=0.5$.

the limit of infinite-size. The position of the inflection point is often used to approximate the bulk phase transition point in Monte Carlo simulations of finite-size samples.

According to our calculations, the inflection point corresponding to the largest parallelepiped simulation can be considered to be a good estimate for the phase transition within the Monte Carlo method. We plotted the temperature of the inflection point, T_N, as a function of $N^{-1/2}$ and observed the limiting value as $N^{-1/2}\rightarrow 0$. This extrapolation of T_N to $N\rightarrow\infty$ hardly differs from the temperature of the inflection point for $N=60^3$.

From Fig. 8 it follows that Monte Carlo simulation for parallelepipeds with periodic boundary conditions ("no surface") is much more appropriate to the bulk behavior than Monte Carlo simulation for the spherical nanoparticle with free boundary conditions. The number of particles $N=20^3=8000$ in the smallest parallelepiped considered is very close to the number $N=8007$ of particles in the spherical nanoparticle (see below Table IV). This large difference in Monte Carlo simulation between parallelepiped and sphere is caused by the difference in shape and boundary conditions.

The temperatures, 1495 K and 1514 K, estimated for the phase transition within the analytical ring approximation[18] and Monte Carlo simulation, respectively, are in close correspondence to the experimental[48] 1572 K. This 4% error demonstrates the adequacy of the mixing potential values at $c=0.5$ calculated from first principles (i.e., without a fitting to experimental data).

In order to test the applicability of these values over the entire concentration interval, we calculated the order-disorder phase transition temperature as a function of concentration within the analytical ring approximation[18] using the mixing potential calculated for $c=0.5$. The corresponding results together with experimental ones are presented in Fig. 9 (see also Fig. 10). From this figure one may conclude that the equiatomic mixing potential is only valid in the vicinity of $c=0.5$. Outside this vicinity it is necessary to use different mixing potentials. The asymmetry of experimental phase diagram with respect to $c=0.5$ implies that the mixing potentials should be concentration dependent and/or nonpair.[26] According to our canonical cluster expansion formalism,[24] within the Connolly-Williams method one should calculate the mixing potentials at any given concentration using structures with the *same* (or close) compositions. Within the KKR-CPA, the concentration dependence of mixing potentials is obtained naturally.

VIII. NANOPARTICLE SIMULATION

The mixing potentials calculated in Sec. III by the Connolly-Williams method were used for Monte Carlo simulations of the temperature dependence of the equilibrium $L1_0$ order parameter of spherical FePt nanoparticles with diameters of 5.94, 3.5, 3.0, and 2.5 nm. In all cases the compositions are close to $c=0.5$. The characteristics of those nanoparticles are listed in Table IV.

Note that the starting configuration for all cases considered was chosen to be a completely ordered one with an $L1_0$ order parameter of unity. The deviations of concentration from equiatomic $c=0.5$ are due to the finite sizes and spherical shape of the nanoparticles.

The results of the simulations are presented in Fig. 11. For spherical nanoparticles, the tendencies in the behavior of order parameter are the same as in case of parallelepipeds (see above Sec. VII). Namely, in case of finite-size particles, instead of a phase transition point (see bulk curve), there is an

TABLE IV. The characteristics of spherical nanoparticles used in Monte Carlo simulation: d, diameter; d/a, ratio of diameter to lattice parameter; N, N_{Fe}, and N_{Pt}, the numbers of sites, iron, and platinum atoms in the sample, respectively; $c=N_{Fe}/N_{Pt}$, concentration; $\bar{\eta}$ and D, the value and dispersion (due to the thermodynamic fluctuations) of order parameter at 600 °C (see Fig. 11); c_{max}, the value of concentration for which the concentrational dependence of $L1_0$ equilibrium order parameter achieves maximum (see Fig. 12).

d (nm)	d/a	N	N_{Fe}	N_{Pt}	c	$\bar{\eta}$	D	c_{max}
5.94	15.63	8007	4007	4000	0.500	0.863	0.007	0.52
3.50	9.21	1601	825	776	0.515	0.839	0.021	0.53
3.00	7.89	1055	519	536	0.492	0.746	0.033	
2.50	6.58	603	299	304	0.496	0.704	0.045	0.56

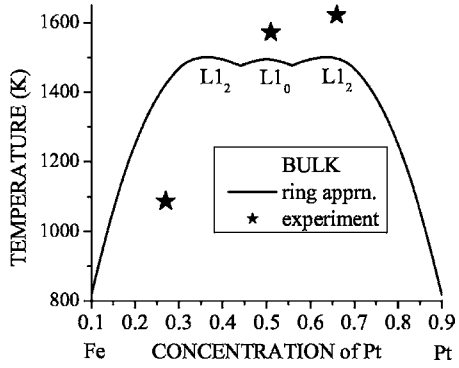

FIG. 9. Bulk configurational T-c phase diagram obtained within the analytical ring approximation (Ref. 18) using mixing potentials calculated by the Connolly-Williams method at $c=0.5$. Lines correspond to phase transitions from disorder to $L1_0$ or $L1_2$ structures with decreasing temperature. Stars correspond to the phase transitions observed experimentally (Ref. 48) (see also Fig. 10).

inflection point. The smaller the particle size, the smoother the $\bar{\eta}(T)$ curve, the less order parameter at low temperatures (below and somewhat above the inflection point), and the higher the order parameter at high temperatures (well above the inflection point). The inflection point temperature decreases with decrease of particle size. Note that in Ref. 36 the same tendencies were observed but the position of the heat capacity maximum was interpreted as a phase transition point. Such an interpretation should be very approximate in case of small finite systems because there is no formal phase transition in a finite system.[5] The same tendencies as in Fig. 11 were observed in Monte Carlo simulations of Cu_3Au nanoparticles in Ref. 51.

Our calculations predict, for example, that 3.5-nm-diam particles in configurational equilibrium at 600 °C would have an order parameter $\bar{\eta}=0.84$ compared to a maximum possible value of unity (see Table IV and Fig. 11). Therefore, annealing at 600 °C will not yield perfect order for 3.5-nm-diam particles. Approximately 17% of the atoms will be on the wrong sublattices, even in equilibrium. The corresponding dispersion of η due to the thermodynamic fluctuations is

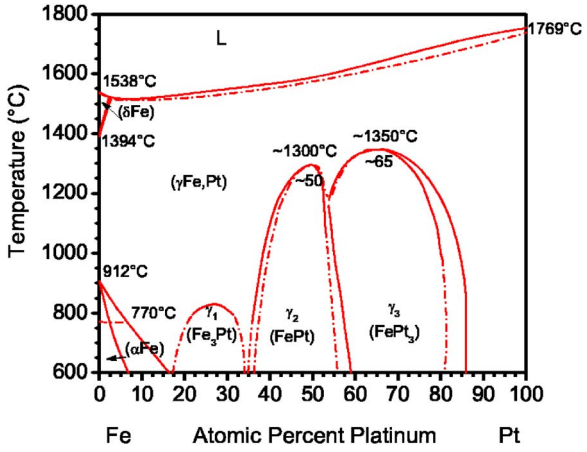

FIG. 10. (Color online) Experimental bulk configurational T-c phase diagram (Ref. 48).

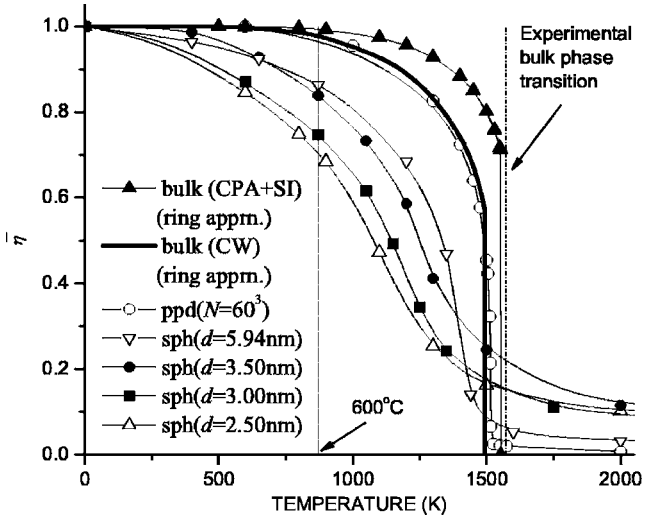

FIG. 11. The temperature dependence of the FePt equilibrium $L1_0$ order parameter $\bar{\eta}$ obtained within the analytical ring approximation (Ref. 18) for bulk ("bulk") using KKR-CPA plus strain-induced interactions at $L=-0.0294$(CPA+SI) and Connolly-Williams mixing potential at $N_s=3, N_\varepsilon=23$ (CW) as well as by Monte Carlo simulation for the parallelepiped ("ppd") sample containing $N=60^3$ atoms and for spherical ("sph") nanoparticles with 2.5, 3.0, 3.5, and 6.0 nm diameters d at equiatomic (or near equiatomic; see Table IV) concentration $c=0.5$ using Connolly-Williams mixing potential.

comparatively small (e.g., 2.5% for $d=3.5$, $T=600$ °C see Table IV).

The "tail" of the order parameter at high temperatures in Fig. 11 is a consequence of thermodynamic fluctuations of the order parameter. The asymptotic behavior of the dispersion of such fluctuations can be estimated as $\sim 1/\sqrt{N}$ (N is the number of atoms).[52] So the value of the high-temperature tail of the order parameter increases with decreasing particle size. Note that we define the order parameter as in Eq. (16), taking into account the fact that two configurations with different signs of the order parameter are physically identical.

Experimentally, nanoparticles are created with some dispersion in the concentration. Therefore it is important to know the concentration dependence of the order parameter. We studied this dependency for the cases of bulk and spherical nanoparticles of different diameters at fixed temperature $T=600$ °C. The corresponding results are presented in Fig. 12. At each concentration we present the *equilibrium* order parameter value so that near concentrations $c=0.5$ and $c=0.25,0.75$ the curves correspond to $L1_0$ and $L1_2$ order parameters, respectively.

From Fig. 12 it follows that for small FePt nanoparticles we observe an asymmetry in the concentration dependence of the order parameter with respect to equiatomic $c=0.5$. This asymmetry is a consequence of the finite size of nanoparticles. It should be emphasized that for the calculation of order parameters in Fig. 12 at each concentration we used the *same* pair mixing potentials as at $c=0.5$ that results in a symmetric order parameter for case of bulk. The concentration dependence of mixing potentials and/or appearance of non pair mixing potentials at $c\neq 0.5$ can make the bulk curve

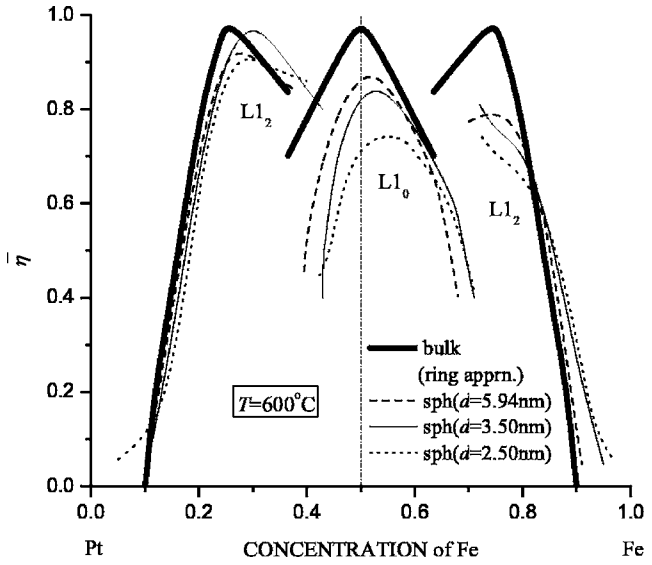

FIG. 12. The concentration dependence of the FePt equilibrium $L1_0$ and $L1_2$ order parameters in bulk ("bulk") and spherical ("sph") nanoparticles with 2.5, 3.5, and 5.94 nm diameters d at fixed temperature $T=600$ °C. The results for bulk and spherical nanoparticles were obtained within the analytical ring approximation (Ref. 18) and by Monte Carlo simulations, respectively, using mixing potentials calculated at $c=0.5$ within the Connolly-Williams method.

asymmetrical[26] and make an additional contribution to the asymmetry for finite particles observed in Fig. 12. One should consider the results in Fig. 12 to be more approximate the farther they are from $c=0.5$.

IX. SURFACE EFFECTS

In our study, we have used mixing potentials obtained for *infinite* bulk alloys and *free* boundary conditions to simulate the equilibrium configuration of *finite*-size particles. The presence of the surface will change the atomic potentials in the near-surface region compared to bulk potentials. This change may result in surface segregation, leading, for example, to the tendency of Fe or Pt atoms to be preferably situated at the surface. In general, surface segregation should decrease the total $L1_0$ order parameter in nanoparticles, because the $L1_0$ order will be reduced at the surface. The surface effect on the order will depend on the ratio of depth of surface segregation to nanoparticle size.

Analytical estimation of such surface effects is not straightforward and will be done elsewhere.[53] Here we only describe the source of the asymmetry observed in Fig. 12. Namely, it is observed that in the presence of a free surface the Connolly-Williams bulk mixing potentials result in weak segregation of Fe atoms to the surface. This causes a depletion of Fe in the interior of the nanoparticle. Thus the effective concentration of Fe atoms within the nanoparticle but outside the surface segregation region will be less than one-half. Therefore it is necessary to add Fe atoms to the interior of the nanoparticle to achieve equiatomic composition outside the segregating surface and accordingly to achieve the maximum $L1_0$ order in that region. That is why the maximum of the $L1_0$ order parameter lies on the Fe-rich side of equiatomic composition in Fig. 12. A similar effect (but for the pseudo phase transition temperature in finite systems[5]) was observed in Ref. 36 for the case in which a strong segregation potential leading to the segregation of Pt to the surface was introduced during Monte Carlo simulation. That additional potential also results in a decrease of total order parameter in accordance with our description above.

For nanoparticles chemically synthesized by methods such as the "hot soap process,"[1] the problem of the effect of the surface on the interatomic exchange potentials is even more complicated because these nanoparticles are likely to have unknown atoms and molecules attached to their surfaces. It should also be noted that truncation of the mixing potentials at a surface is an uncontrolled approximation. The fact that our simulations yield segregation of Fe to the surface should not be taken as evidence that this would happen for a real nanoparticle. Indeed our own preliminary first-principles calculations indicate that Pt (rather than Fe) segregates to a (001) surface, a result that appears to be consistent with recent unpublished work by Yang *et al.*[36] A more complete treatment of surface segregation in isolated nanoparticles will be published elsewhere.[53]

X. CONCLUSIONS AND DISCUSSION

In the present paper, the pair mixing potentials (which determine the alloy configurational behavior) were calculated up to the third coordination shell for equiatomic FePt alloys from first principles using the Connolly-Williams method (Sec. III). It was shown that the application of this method does not necessarily lead to significant nonpair interactions if all of the structures employed in the Connolly-Williams method correspond to the same composition (canonical cluster expansion formalism[24]). The mixing potential was also calculated by adding the strain-induced part of the interactions to mixing potentials obtained from the KKR-CPA approach of Ref. 16 (Sec. V). The application of the Connolly-Williams method at fixed composition allowed the direct comparison of these potentials with those obtained from the KKR-CPA (plus strain-induced part). The mixing potentials are shown to be similar with both giving values for the order-disorder phase transition very close to the experimental one. It was demonstrated that, in the considered alloy, the Connolly-Williams potentials (based on completely *ordered* states) and the KKR-CPA potentials (corresponding to completely *disordered* state) can be brought into very close correspondence to each other simply by increasing the magnitude of the strain-induced interactions added to KKR-CPA potential (Sec. V).

It should be emphasized that it was not clear *a priori* that either the Connolly-Williams method or the CPA approach could be trusted for a system as complicated as FePt. Magnetic alloys are problematic for the Connolly-Williams method because the mixing potentials are strongly dependent on the magnetic state of the system. Thus the chemical order and magnetic structure are expected to be intimately related. On the other hand, the CPA approach is based on concentra-

tion fluctuations in a hypothetical high-temperature disordered state. We consider the fact that both methods are able to approximate the order-disorder temperature well without adjustable parameters and that the mixing potentials derived from the two approaches are rather similar to be a remarkable result. It demonstrates the possibility of using these potentials with comparatively small error even in a region, where our assumptions about these potentials are not valid.

It was shown by first-principles calculations that parallel $L1_0$ antiphase boundaries are not energetically favorable (Sec. IV). This fact demonstrates the inapplicability of the nearest-neighbor interaction model in accordance with Connolly-Williams and KKR-CPA results. The absence of parallel $L1_0$ antiphase boundaries was confirmed by Monte Carlo simulations using the Connolly-Williams potential (Secs. VII and VIII).

In Secs. VII and VIII, the mixing potentials obtained by the Connolly-Williams method were used to investigate the dependence of equilibrium $L1_0$ ordering on temperature for bulk and for spherical nanoparticles with diameters of 5.94, 3.5, 3.0, and 2.5 nm. These calculations used both Monte Carlo simulations and the analytical ring approximation. The calculated order-disorder temperature for bulk (1495–1514 K) was in relatively good agreement (4% error) with the experimental value (1572 K). For nanoparticles of finite size, the (long-range) order parameter changed continuously from unity to finite asymptotic values with increasing temperature. The nonzero asymptotic values are a consequence of thermodynamic fluctuations of the order parameter and are proportional to $1/\sqrt{N}$ where N is the number of atoms in a sample. Rather than a discontinuity indicative of a phase transition, we obtained an inflection point (a precursor of a phase transition at large size) in the $L1_0$ order as a function of temperature. This inflection point occurred at a temperature below the bulk phase transition temperature and which decreased as the particle size decreased.

According to our investigations, the experimental absence of (relatively) high order in nanoparticles below 600 °C is primarily a *kinetic* problem rather than an equilibrium one. For example, our calculations predict, that 3.5-nm-diam particles in configurational equilibrium at 600 °C (a typical annealing temperature for promoting $L1_0$ ordering) have an $L1_0$ order parameter of 0.84 (compared to a maximum possible value equal to unity). It should be noted that to rapidly obtain the correct equilibrium state, we used simplified kinetics in our Monte Carlo simulation. Namely, we allowed *any* two randomly chosen atoms to exchange their positions *without* an additional diffusion barrier. In a real alloy, the main mechanism of atomic diffusion is much slower because it consists of the exchange of the positions of atoms and neighboring vacancies through energy barriers. Moreover, at each temperature we started the simulation from the completely ordered state, whereas the actual nanoparticles are initially prepared in the disordered state and the transformation from the disordered to the ordered state may be much slower than the reverse one, especially at low temperatures. Nevertheless, even with our simplified kinetics, we observed a slowing-down problem in approaching the equilibrium ordered state at low temperatures. In real nanoparticles this problem must be much worse. Kinetic acceleration methods such as irradiation and/or addition of other types of atoms may be useful in accelerating the formation of long range order. Kang *et al.*[54] *have* observed ordering on annealing at temperatures somewhat below 400 °C by adding Ag or Au to the particles in the synthesis step. However, it appears that this ordering is also accompanied by agglomeration and sintering of the particles. It should be emphasized that all of the results presented in this paper correspond to equilibrium states and are, therefore, independent of the particular kinetic pathways that lead to these states.

In Sec. VIII, it was demonstrated that for small finite samples even for a composition-independent, pair mixing potential one obtains an asymmetric order parameter as a function of composition with respect to equiatomic composition. In particular, for FePt nanoparticles, if we neglect the effect of the surface on the mixing potentials, the maximum of the $L1_0$ order parameter as a function of composition is shifted from $c=0.5$ toward the Fe-rich region. The connection of such an asymmetry with surface segregation is discussed in Sec. IX. Also in Sec. IX the importance of the consideration of the surface segregation effect on the atomic ordering is pointed out (such a consideration will be done elsewhere[53]).

ACKNOWLEDGMENTS

This research was supported by the Defense Advanced Research Projects Agency through ONR Contract No. N00014-02-01-0590 and by the National Science Foundation through MRSEC Grant Nos. DMR0213985 and NSF SA4130-10092PG/82939. The authors thank Professor J.W. Harrell for stimulating discussions and Dr. J. Velev for participation in early stages of the present work. Special thanks to Professor J. B. Staunton for providing us the numerical values of KKR-CPA-based mixing potential calculated in Ref. 16. We are grateful to Professor M. Asta and Dr. O. N. Mryasov for communicating their results prior to publication.

APPENDIX: DEFINITION OF STRUCTURES

The present appendix (Table V and subsections 1–28 below), defines the structures used in this paper. Unit-cell basis vectors are given in Cartesian coordinates in units of the fcc lattice parameter. The Cartesian axes are directed along the edges of the fcc cube. The third unit-cell basis vector is perpendicular to the first and second ones for all structures. All of the structures have equiatomic composition $c=0.5$. The atom positions in the tables are before relaxation. In addition to numbering, we also include the structure designations that we used during our calculations. For the 1st, 2nd, and 24th structures we put also the designations known in the literature ("$L1_0$," "CH(40)," and "Z2," respectively).[55] The first 23 structures are linearly independent and were used in the Connolly-Williams method in Sec. III. The remaining 5 structures are linearly dependent (but not identical) to the first 23 ones. They were considered in order to check the predictive power of the Connolly-Williams potentials.

TABLE V. The characteristics of the structures used in the paper. i is the structure number, $N_{\mathrm{u.c.}}^{AB}$ is the total number of atoms in the unit cell of structure, $E_{\mathrm{u.c.}}$ is the energy of structure per its unit cell (as obtained from VASP calculations), $V_{\mathrm{u.c.}}^{(0)}$ is the energy (per unit cell) of the structure with the same unit cell but with Fe atoms only (see Sec. II), and S_{is} are the structural coefficients ($i=1,2\ldots,28$, $s=1,2\ldots,8$) in the Connolly-Williams system of equations (9). Note that the values of ε_i [see Eqs. (9) and (10)] can be determined from this table as $\varepsilon_i=(E_{\mathrm{u.c.}}-V_{\mathrm{u.c.}}^{(0)})/N_{\mathrm{u.c.}}^{AB}$, where the values on the right side of this equation correspond to the ith structure.

i	$N_{\mathrm{u.c.}}^{AB}$	$V_{\mathrm{u.c.}}^{(0)}$	$E_{\mathrm{u.c.}}$	$S_{is}\times N_{\mathrm{u.c.}}^{AB}$							
1	16	−129.0729	−117.0299	16	24	32	48	32	32	64	24
2			−116.1764	16	16	64	16	32	0	128	24
3			−116.6366	16	20	48	32	32	16	96	16
4			−114.5503	40	20	64	32	64	16	96	16
5			−114.9625	34	20	60	32	54	16	92	18
6			−114.6047	36	20	64	32	56	16	96	16
7	16	−129.0250	−115.4097	27	14	38	24	54	8	76	24
8			−115.2592	28	14	40	16	56	8	80	24
9	18	−145.2008	−130.8012	22	23	44	42	36	28	88	23
10			−130.8094	22	23	40	42	44	28	84	23
11			−131.0869	20	23	44	42	42	28	84	23
12	10	−80.6305	−72.2655	14	9	26	12	34	8	66	9
13	8	−64.5151	−57.1224	18	8	28	12	20	8	40	4
14			−57.7453	13	6	26	10	22	12	44	8
15	6	−48.3836	−43.0543	12	5	16	8	12	8	32	5
16	12	−96.7403	−85.1600	30	14	52	24	44	16	80	10
17			−85.7956	25	12	46	20	38	16	72	10
18	12	−96.7380	−86.9505	16	10	32	16	40	16	80	10
19	12	−96.7780	−86.6918	20	10	30	18	38	8	58	14
20	8	−64.5043	−58.1203	10	8	20	12	28	8	56	4
21	20	−161.2637	−144.2564	35	18	47	24	74	8	93	26
22			−144.1195	36	18	46	22	76	6	94	26
23	16	−129.0224	−115.4658	28	14	38	22	54	8	76	20
24	8	−64.5283	−57.6927	16	8	16	8	32	0	32	12
25			−57.8895	12	10	16	16	24	8	32	12
26			−57.7018	12	8	24	8	24	0	48	12
27			−58.1095	10	10	20	16	20	8	40	12
28			−58.2748	8	10	24	16	16	8	48	12

1. 4cub(1), $L1_0$

Unit cell basis vectors Cartesian coordinates:
(1.0,0.0,0.0), (0.0,1.0,0.0), (0.0,0.0,4.0).
Atomic Cartesian coordinates:
A: (0.0,0.0,0.0), (0.5,0.5,0.0), (0.0,0.0,1.0), (0.5,0.5,1.0), (0.0,0.0,2.0), (0.5,0.5,2.0), (0.0,0.0,3.0), (0.5,0.5,3.0).
B: (0.5,0.0,0.5), (0.0,0.5,0.5), (0.5,0.0,1.5), (0.0,0.5,1.5), (0.5,0.0,2.5), (0.0,0.5,2.5), (0.5,0.0,3.5), (0.0,0.5,3.5).

2. 4cub(2), APB(1), CH(40)

Unit cell basis vectors Cartesian coordinates:
(1.0,0.0,0.0), (0.0,1.0,0.0), (0.0,0.0,4.0).
Atomic Cartesian coordinates:
A: (0.0,0.0,0.0), (0.5,0.0,0.5), (0.5,0.5,1.0), (0.0,0.5,1.5), (0.0,0.0,2.0), (0.5,0.0,2.5), (0.5,0.5,3.0), (0.0,0.5,3.5).
B: (0.5,0.5,0.0), (0.0,0.5,0.5), (0.0,0.0,1.0), (0.5,0.0,1.5), (0.5,0.5,2.0), (0.0,0.5,2.5), (0.0,0.0,3.0), (0.5,0.0,3.5).

3. 4cub(3), APB(2)

Unit cell basis vectors Cartesian coordinates:
(1.0,0.0,0.0), (0.0,1.0,0.0), (0.0,0.0,4.0).
Atomic Cartesian coordinates:
A: (0.0,0.0,0.0), (0.5,0.0,0.5), (0.0,0.0,1.0), (0.5,0.0,1.5), (0.5,0.5,2.0), (0.0,0.5,2.5), (0.5,0.5,3.0), (0.0,0.5,3.5).
B: (0.5,0.5,0.0), (0.0,0.5,0.5), (0.5,0.5,1.0), (0.0,0.5,1.5), (0.0,0.0,2.0), (0.5,0.0,2.5), (0.0,0.0,3.0), (0.5,0.0,3.5).

4. 4cub(4)

Unit cell basis vectors Cartesian coordinates:
(1.0,0.0,0.0), (0.0,1.0,0.0), (0.0,0.0,4.0).

Atomic Cartesian coordinates:
A: (0.0,0.0,0.0), (0.5,0.5,0.0), (0.5,0.0,0.5), (0.0,0.5,0.5), (0.0,0.0,1.0), (0.5,0.5,1.0), (0.5,0.0,1.5), (0.0,0.5,1.5).
B: (0.0,0.0,2.0), (0.5,0.5,2.0), (0.5,0.0,2.5), (0.0,0.5,2.5), (0.0,0.0,3.0), (0.5,0.5,3.0), (0.5,0.0,3.5), (0.0,0.5,3.5).

5. 4cub(5)

Unit cell basis vectors Cartesian coordinates:
(1.0,0.0,0.0), (0.0,1.0,0.0), (0.0,0.0,4.0).
Atomic Cartesian coordinates:
A: (0.0,0.0,0.0), (0.5,0.5,0.0), (0.5,0.0,0.5), (0.0,0.5,0.5), (0.0,0.0,1.0), (0.5,0.5,1.0), (0.5,0.0,1.5), (0.0,0.0,2.0).
B: (0.0,0.5,1.5), (0.5,0.5,2.0), (0.5,0.0,2.5), (0.0,0.5,2.5), (0.0,0.0,3.0), (0.5,0.5,3.0), (0.5,0.0,3.5), (0.0,0.5,3.5).

6. 4cub(6)

Unit cell basis vectors Cartesian coordinates:
(1.0,0.0,0.0), (0.0,1.0,0.0), (0.0,0.0,4.0).
Atomic Cartesian coordinates:
A: (0.0,0.0,0.0), (0.5,0.5,0.0), (0.5,0.0,0.5), (0.0,0.5,0.5), (0.0,0.0,1.0), (0.5,0.5,1.0), (0.5,0.0,1.5), (0.0,0.5,3.5).
B: (0.0,0.5,1.5), (0.0,0.0,2.0), (0.5,0.5,2.0), (0.5,0.0,2.5), (0.0,0.5,2.5), (0.0,0.0,3.0), (0.5,0.5,3.0), (0.5,0.0,3.5).

7. 4ppd1-2pl(1)

Unit cell basis vectors Cartesian coordinates:
(1.0,−1.0,0.0), (1.0,1.0,0.0), (0.0,0.0,2.0).
Atomic Cartesian coordinates:
A: (0.0,0.0,0.0), (0.5,−0.5,0.0), (0.5,0.5,0.0), (1.0,0.0,0.0), (0.5,0.0,0.5), (1.0,−0.5,0.5), (1.0,0.5,0.5), (0.0,0.0,1.0).
B: (1.5,0.0,0.5), (0.5,−0.5,1.0), (0.5,0.5,1.0), (1.0,0.0,1.0), (0.5,0.0,1.5), (1.0,−0.5,1.5), (1.0,0.5,1.5), (1.5,0.0,1.5).

8. 4ppd1-2pl(2)

Unit cell basis vectors Cartesian coordinates:
(1.0,−1.0,0.0), (1.0,1.0,0.0), (0.0,0.0,2.0).
Atomic Cartesian coordinates:
A: (0.0,0.0,0.0), (0.5,−0.5,0.0), (0.5,0.5,0.0), (1.0,0.0,0.0), (0.5,0.0,0.5), (1.0,−0.5,0.5), (1.0,0.5,0.5), (0.5,0.0,1.5).
B: (1.5,0.0,0.5), (0.0,0.0,1.0), (0.5,−0.5,1.0), (0.5,0.5,1.0), (1.0,0.0,1.0), (1.0,−0.5,1.5), (1.0,0.5,1.5), (1.5,0.0,1.5).

9. 9ppd1-1pl(1)

Unit cell basis vectors Cartesian coordinates:
(1.5,−1.5,0.0), (1.5,1.5,0.0), (0.0,0.0,1.0).
Atomic Cartesian coordinates:
A: (0.0,0.0,0.0), (0.5,−0.5,0.0), (1.0,−1.0,0.0), (0.5,0.5,0.0), (1.0,0.0,0.0), (1.5,−0.5,0.0), (1.0,1.0,0.0), (1.5,0.5,0.0), (0.5,0.0,0.5).
B: (2.0,0.0,0.0), (1.0,−0.5,0.5), (1.5,−1.0,0.5), (1.0,0.5, 0.5), (1.5,0.0,0.5), (2.0,−0.5,0.5), (1.5,1.0,0.5), (2.0,0.5,0.5), (2.5,0.0,0.5).

10. 9ppd1-1pl(2)

Unit cell basis vectors Cartesian coordinates:
(1.5,−1.5,0.0), (1.5,1.5,0.0), (0.0,0.0,1.0).
Atomic Cartesian coordinates:
A: (0.0,0.0,0.0), (0.5,−0.5,0.0), (1.0,−1.0,0.0), (0.5,0.5, 0.0), (1.0,0.0,0.0), (1.5,−0.5,0.0), (1.0,1.0,0.0), (1.5,0.5,0.0), (1.0,−0.5,0.5).
B: (2.0,0.0,0.0), (0.5,0.0,0.5), (1.5,−1.0,0.5), (1.0,0.5,0.5), (1.5,0.0,0.5), (2.0,−0.5,0.5), (1.5,1.0,0.5), (2.0,0.5,0.5), (2.5,0.0,0.5).

11. 9ppd1-1pl(3)

Unit cell basis vectors Cartesian coordinates:
(1.5,−1.5,0.0), (1.5,1.5,0.0), (0.0,0.0,1.0).
Atomic Cartesian coordinates:
A: (0.0,0.0,0.0), (0.5,−0.5,0.0), (1.0,−1.0,0.0), (0.5,0.5,0.0), (1.0,0.0,0.0), (1.5,−0.5,0.0), (1.0,1.0,0.0), (1.5,0.5,0.0), (1.5,0.0,0.5).
B: (2.0,0.0,0.0), (0.5,0.0,0.5), (1.0,−0.5,0.5), (1.5, −1.0,0.5), (1.0,0.5,0.5), (2.0,−0.5,0.5), (1.5,1.0,0.5), (2.0, 0.5,0.5), (2.5,0.0,0.5).

12. 1ppd2-1pl

Unit cell basis vectors Cartesian coordinates:
(1.5,−0.5,0.0), (0.5,1.5,0.0), (0.0,0.0,1.0).
Atomic Cartesian coordinates:
A: (0.0,0.0,0.0), (0.5,0.0,0.5), (0.5,0.5,0.0), (1.0,0.0,0.0), (1.0,0.5,0.5).
B: (0.5,1.0,0.5), (1.0,1.0,0.0), (1.5,0.0,0.5), (1.5,0.5,0.0), (1.5,1.0,0.5).

13. 2ppd3a-1pl(1)

Unit cell basis vectors Cartesian coordinates:
(3.0,−1.0,0.0), (0.5,0.5,0.0), (0.0,0.0,1.0).
Atomic Cartesian coordinates:
A: (0.0,0.0,0.0), (0.5,0.0,0.5), (1.0,0.0,0.0), (1.5,0.0,0.5).
B: (1.5,−0.5,0.0), (2.0,−0.5,0.5), (2.5,−0.5,0.0), (3.0, −0.5,0.5).

14. 2ppd3a-1pl(2)

Unit cell basis vectors Cartesian coordinates:
(3.0,−1.0,0.0), (0.5,0.5,0.0), (0.0,0.0,1.0).
Atomic Cartesian coordinates:
A: (0.0,0.0,0.0), (0.5,0.0,0.5), (1.0,0.0,0.0), (2.0,−0.5,0.5).
B: (1.5,0.0,0.5), (1.5,−0.5,0.0), (2.5,−0.5,0.0), (3.0, −0.5,0.5).

15. 1ppd4-1pl

Unit cell basis vectors Cartesian coordinates:
(2.0,−1.0,0.0), (0.5,0.5,0.0), (0.0,0.0,1.0).
Atomic Cartesian coordinates:
A: (0.0,0.0,0.0), (0.5,0.0,0.5), (1.0,0.0,0.0).
B: (1.0,−0.5,0.5), (1.5,−0.5,0.0), (2.0,−0.5,0.5).

16. 2ppd4a-1pl(1)

Unit cell basis vectors Cartesian coordinates:
(4.0,−2.0,0.0), (0.5,0.5,0.0), (0.0,0.0,1.0).
Atomic Cartesian coordinates:
A: (0.0,0.0,0.0), (0.5,0.0,0.5), (1.0,0.0,0.0), (1.0,−0.5,0.5), (1.5,−0.5,0.0), (2.0,−0.5,0.5).
B: (2.0,−1.0,0.0), (2.5,−1.0,0.5), (3.0,−1.0,0.0), (3.0,−1.5,0.5), (3.5,−1.5,0.0), (4.0,−1.5,0.5).

17. 2ppd4a-1pl(2)

Unit cell basis vectors Cartesian coordinates:
(4.0,−2.0,0.0), (0.5,0.5,0.0), (0.0,0.0,1.0).
Atomic Cartesian coordinates:
A: (0.0,0.0,0.0), (0.5,0.0,0.5), (1.0,0.0,0.0), (1.0,−0.5,0.5), (1.5,−0.5,0.0), (2.5,−1.0,0.5).
B: (2.0,−0.5,0.5), (2.0,−1.0,0.0), (3.0,−1.0,0.0), (3.0,−1.5,0.5), (3.5,−1.5,0.0), (4.0,−1.5,0.5).

18. 2ppd4b-1pl

Unit cell basis vectors Cartesian coordinates:
(2.0,−1.0,0.0), (1.0,1.0,0.0), (0.0,0.0,1.0).
Atomic Cartesian coordinates:
A: (0.0,0.0,0.0), (0.5,0.0,0.5), (1.0,0.0,0.0), (1.0,−0.5,0.5), (1.5,−0.5,0.0), (2.0,−0.5,0.5).
B: (0.5,0.5,0.0), (1.0,0.5,0.5), (1.5,0.5,0.0), (1.5,0.0,0.5), (2.0,0.0,0.0), (2.5,0.0,0.5).

19. 1ppd4-2pl

Unit cell basis vectors Cartesian coordinates:
(2.0,−1.0,0.0), (0.5,0.5,0.0), (0.0,0.0,2.0).
Atomic Cartesian coordinates:
A: (0.0,0.0,0.0), (0.5,0.0,0.5), (1.0,0.0,0.0), (1.0,−0.5,0.5), (1.5,−0.5,0.0), (0.0,0.0,1.0).
B: (2.0,−0.5,0.5), (0.5,0.0,1.5), (1.0,0.0,1.0), (1.0,−0.5,1.5), (1.5,−0.5,1.0), (2.0,−0.5,1.5).

20. 2ppd3b-1pl

Unit cell basis vectors Cartesian coordinates:
(1.5,−0.5,0.0), (1.0,1.0,0.0), (0.0,0.0,1.0).
Atomic Cartesian coordinates:
A: (0.0,0.0,0.0), (0.5,0.0,0.5), (1.0,0.0,0.0), (1.5,0.0,0.5).
B: (0.5,0.5,0.0), (1.0,0.5,0.5), (1.5,0.5,0.0), (2.0,0.5,0.5).

21. 1ppd2-2pl(1)

Unit cell basis vectors Cartesian coordinates:
(1.5,−0.5,0.0), (0.5,1.5,0.0), (0.0,0.0,2.0).
Atomic Cartesian coordinates:
A: (0.0,0.0,0.0), (0.5,0.0,0.5), (0.5,0.5,0.0), (0.5,1.0,0.5), (1.0,0.0,0.0), (1.0,0.5,0.5), (1.0,1.0,0.0), (1.5,0.0,0.5), (1.5,0.5,0.0), (0.0,0.0,1.0).
B: (1.5,1.0,0.5), (0.5,0.0,1.5), (0.5,0.5,1.0), (0.5,1.0,1.5), (1.0,0.0,1.0), (1.0,0.5,1.5), (1.0,1.0,1.0), (1.5,0.0,1.5), (1.5,0.5,1.0), (1.5,1.0,1.5).

22. 1ppd2-2pl(2)

Unit cell basis vectors Cartesian coordinates:
(1.5,−0.5,0.0), (0.5,1.5,0.0), (0.0,0.0,2.0).
Atomic Cartesian coordinates:
A: (0.0,0.0,0.0), (0.5,0.0,0.5), (0.5,0.5,0.0), (0.5,1.0,0.5), (1.0,0.0,0.0), (1.0,0.5,0.5), (1.0,1.0,0.0), (1.5,0.0,0.5), (1.5,0.5,0.0), (0.5,0.0,1.5).
B: (1.5,1.0,0.5), (0.0,0.0,1.0), (0.5,0.5,1.0), (0.5,1.0,1.5), (1.0,0.0,1.0), (1.0,0.5,1.5), (1.0,1.0,1.0), (1.5,0.0,1.5), (1.5,0.5,1.0), (1.5,1.0,1.5).

23. 2ppd3-3c-2pl

Unit cell basis vectors Cartesian coordinates:
(3.5,−0.5,0.0), (0.5,0.5,0.0), (0.0,0.0,2.0).
Atomic Cartesian coordinates:
A: (0.0,0.0,0.0), (0.5,0.0,0.5), (1.0,0.0,0.0), (1.5,0.0,0.5), (2.0,0.0,0.0), (2.5,0.0,0.5), (3.0,0.0,0.0), (0.0,0.0,1.0).
B: (3.5,0.0,0.5), (0.5,0.0,1.5), (1.0,0.0,1.0), (1.5,0.0,1.5), (2.0,0.0,1.0), (2.5,0.0,1.5), (3.0,0.0,1.0), (3.5,0.0,1.5).

24. 2cub(1), Z2

Unit cell basis vectors Cartesian coordinates:
(1.0,0.0,0.0), (0.0,1.0,0.0), (0.0,0.0,2.0).
Atomic Cartesian coordinates:
A: (0.0,0.0,0.0), (0.5,0.5,0.0), (0.5,0.0,0.5), (0.0,0.5,0.5).
B: (0.0,0.0,1.0), (0.5,0.5,1.0), (0.5,0.0,1.5), (0.0,0.5,1.5).

25. 2cub(2)

Unit cell basis vectors Cartesian coordinates:
(1.0,0.0,0.0), (0.0,1.0,0.0), (0.0,0.0,2.0).
Atomic Cartesian coordinates:
A: (0.0,0.0,0.0), (0.5,0.5,0.0), (0.5,0.0,0.5), (0.5,0.0,1.5).
B: (0.0,0.5,0.5), (0.0,0.0,1.0), (0.5,0.5,1.0), (0.0,0.5,1.5).

26. 2cub(3)

Unit cell basis vectors Cartesian coordinates:
(1.0,0.0,0.0), (0.0,1.0,0.0), (0.0,0.0,2.0).
Atomic Cartesian coordinates:
A: (0.0,0.0,0.0), (0.5,0.5,0.0), (0.5,0.0,0.5), (0.0,0.5,1.5).
B: (0.0,0.5,0.5), (0.0,0.0,1.0), (0.5,0.5,1.0), (0.5,0.0,1.5).

27. 2cub(4)

Unit cell basis vectors Cartesian coordinates:
(1.0,0.0,0.0), (0.0,1.0,0.0), (0.0,0.0,2.0).
Atomic Cartesian coordinates:
A: (0.0,0.0,0.0), (0.5,0.5,0.0), (0.5,0.0,0.5), (0.0,0.0,1.0).
B: (0.0,0.5,0.5), (0.5,0.5,1.0), (0.5,0.0,1.5), (0.0,0.5,1.5).

28. 2cub(5)

Unit cell basis vectors Cartesian coordinates:
(1.0,0.0,0.0), (0.0,1.0,0.0), (0.0,0.0,2.0).
Atomic Cartesian coordinates:
A: (0.0,0.0,0.0), (0.5,0.0,0.5), (0.0,0.0,1.0), (0.0,0.5,1.5).
B: (0.5,0.5,0.0), (0.0,0.5,0.5), (0.5,0.5,1.0), (0.5,0.0,1.5).

*Electronic address: r_chepulskii@yahoo.com

[1] S. Sun, C. B. Murray, D. Weller, L. Folks, and A. Moser, Science **287**, 1989 (2000).

[2] Y. K. Takahashi, T. Ohkubo, M. Ohnuma, and K. Hono, J. Appl. Phys. **93**, 7166 (2003).

[3] Annealing at ~600 °C results in sintering of nanoparticles into larger agglomerates which is not desirable for high-density magnetic recording.

[4] $L1_0$ is an fcc tetragonal structure, in which atoms of two types form layers occupying alternating (001) or (010) or (001) planes of the original fcc lattice.

[5] O. G. Mouritsen, *Computer Studies of Phase Transitions and Critical Phenomena* (Springer-Verlag, Berlin, 1984), Sec. 2.2.8.

[6] Some preliminary results of the present paper were presented at the Magnetism and Magnetic Materials Conference, 2004, and will be published in the proceedings of the conference: R. V. Chepulskii, J. Velev, and W. H. Butler, J. Appl. Phys. **97**, 10J311 (2005).

[7] J. W. D. Connolly and A. R. Williams, Phys. Rev. B **27**, 5169 (1983); D. de Fontaine, Solid State Phys. **47**, 33 (1994); A. Zunger, in *Statics and Dynamics of Alloy Phase Transformations*, edited by P. Turchi and A. Gonis (Plenum, New York, 1994), pp. 361–419; A. Zunger, L. Wang, G. Hart, and M. Sanati, Modell. Simul. Mater. Sci. Eng. **10**, 1 (2002); S. Müller, J. Phys.: Condens. Matter **15**, R1429 (2003); V. Blum and A. Zunger, Phys. Rev. B **70**, 155108 (2004).

[8] A. van de Walle and G. Ceder, J. Phase Equilib. **23**, 348 (2002).

[9] We use the term "Connolly-Williams method" to describe a procedure for extracting mixing potential values from the known energies of a set of structures acknowledging the authors who first applied this method. Significant modifications have been made to this approach by later authors including the modifications described in this paper. Other names for this approach for obtaining mixing potentials are "structure inversion method" and "cluster expansion method" (Refs. 7 and 8).

[10] F. Ducastelle, *Order and Phase Stability in Alloys* (Elsevier, New York, 1991).

[11] G. Kresse and J. Furthmuller, Comput. Mater. Sci. **6**, 15 (1996); Phys. Rev. B **54**, 11169 (1996); G. Kresse and D. Joubert, *ibid.* **59**, 1758 (1999).

[12] B. L. Györffy, and G. M. Stocks, Phys. Rev. Lett. **50**, 374 (1983).

[13] D. D. Johnson, D. M. Nicholson, F. J. Pinski, B. L. Györffy, and G. M. Stocks, Phys. Rev. B **41**, 9701 (1990).

[14] J. B. Staunton, D. D. Johnson, and F. J. Pinski, Phys. Rev. B **50**, 1450 (1994).

[15] F. J. Pinski, J. B. Staunton, and D. D. Johnson, Phys. Rev. B **57**, 15177 (1998).

[16] S. Ostanin, S. S. A. Razee, J. B. Staunton, B. Ginatempo, and Ezio Bruno, J. Appl. Phys. **93**, 453 (2003).

[17] N. Metropolis, A. W. Rosenbluth, M. N. Rosenbluth, A. H. Teller, and E. Teller, J. Chem. Phys. **21**, 1087 (1953); M. E. J. Newman and G. T. Barkema, *Monte Carlo Methods in Statistical Physics* (Oxford University Press, Oxford, 1999), Sec. 3.1.

[18] R. V. Chepulskii, Solid State Commun. **115**, 497 (2000); Phys. Rev. B **69**, 134431 (2004).

[19] T. D. Lee and C. N. Yang, Phys. Rev. **87**, 410 (1952).

[20] M. A. Krivoglaz and A. A. Smirnov, *The Theory of Order-Disorder in Alloys* (Macdonald, London, 1964); A. G. Khachaturyan, Prog. Mater. Sci. **22**, 1 (1978); D. de Fontaine, Solid State Phys. **34**, 73 (1979).

[21] V. N. Bugaev and R. V. Chepulskii, Acta Crystallogr., Sect. A: Found. Crystallogr. **51**, 456 (1995).

[22] J. M. Sanchez, F. Ducastelle, and D. Gratias, Physica A **128**, 334 (1984).

[23] R. V. Chepulskii, J. B. Staunton, Ezio Bruno, B. Ginatempo, and D. D. Johnson, Phys. Rev. B **65**, 064201 (2001).

[24] M. Asta, C. Wolverton, D. de Fontaine, and H. Dreyssé, Phys. Rev. B **44**, 4907 (1991); C. Wolverton, M. Asta, H. Dreyssé, and D. de Fontaine, *ibid.* **44**, 4914 (1991).

[25] N. A. Zarkevich, D. D. Johnson, and A. V. Smirnov, Acta Mater. **50**, 2443 (2002).

[26] R. V. Chepulskii, J. Phys.: Condens. Matter **10**, 1505 (1998), Sec. 5.

[27] JCPDS-International Centre for Diffraction Data, 1999.

[28] N. A. Zarkevich and D. D. Johnson, Phys. Rev. Lett. **92**, 255702 (2004).

[29] The use of that number of fitting parameters within the Connolly-Williams method that provides a minimum of cross-validation error allows one to avoid "under" or "over" fitting and results in the highest predictive power of the Connolly-Williams method (see Sec. 3.1.1 in Ref. 8.

[30] We found the mixing potential values for shells greater than the third one to be so small that their accurate calculation requires an increase in the accuracy of the VASP calculations and the consideration of many more structures. It is important that the accuracy of the Connolly-Williams structure energy fitting was hardly affected by such an increase of the number of fitting parameters (see Fig. 2).

[31] It should be noted that we found the bulk order-disorder phase transition temperature to be sensitive to small changes in the energies of structures calculated from first principles. For example, the change in ε_i of 10 meV can cause the phase transition temperature to change by 50 K. Taking into account the approximations used at first-principles calculations within the VASP code (generalized gradient approximation to density-functional theory, neglect of lattice vibrations and electronic excitations, etc.), one should realize the corresponding error of statistical calculations based on those calculations.

[32] Comparing Figs. 1 and 5 with Table III, one may conclude that the phase transition temperature is very sensitive to small changes of the mixing potential. At the same time very different mixing potentials may give similar phase transition temperatures. So generally one should be cautious in inferring mixing potentials from the experimental value of the phase transition temperature.

[33] A. G. Khachaturyan, Fiz. Tverd. Tela (Leningrad) **9**, 2861 (1967) [Sov. Phys. Solid State **9**, 2249 (1968)]; Prog. Mater. Sci. **22**, 1 (1978); *Theory of Structural Transformations in Solids* (Wiley, New York, 1983).

[34] M. A. Krivoglaz, Zh. Eksp. Teor. Fiz. **34**, 204 (1958); *The Theory of X-Ray and Thermal Neutron Scattering From Real Crystals* (Plenum, New York, 1969); *Diffuse Scattering of X-rays and Thermal Neutrons by Fluctuational Inhomogeneities of Imperfect Crystals* (Springer, Berlin, 1996).

[35] Y. Chen, S. Iwata, and T. Mohri, CALPHAD: Comput. Coupling Phase Diagrams Thermochem. **26**, 583 (2002).

[36] B. Yang, M. Asta, O. N. Mryasov, T. Klemmer, and R. Chantrell, Scr. Mater. **53**, 417 (2005).

[37] In Ref. 16, two types of the KKR-CPA mixing potentials corresponding to paramagnetic and ferromagnetic states were ob-

tained. Using those paramagnetic and ferromagnetic potentials we correspondingly obtained 1610 K and 1464 K for the structural phase transition temperatures within the ring approximation (Ref. 18). If we add strain-induced interactions (see Sec. V), they are 1552 K and 1406 K, respectively (see also Table III). In the present paper (mainly in Sec. V) we use only *paramagnetic* type of CPA-KKR potential because of the better reproduction of the experimental phase transition temperature. The better correspondence of the *paramagnetic* potential to the experimental data was also obtained in case of $Co_{0.25}Pt_{0.75}$ alloy in A. V. Ruban, S. Shalleross, S. I. Simak, and H. L. Skriver, Phys. Rev. B **70**, 125115 (2004). Note that the phase transition *critical* temperatures presented in Ref. 16 (1975 and 1575 K with paramagnetic and ferromagnetic potentials, respectively) contain errors [J. B. Staunton (private communication)].

[38] T. J. Matsubara, J. Phys. Soc. Jpn. **7**, 270 (1952).

[39] H. Kanzaki, J. Phys. Chem. Solids **2**, 24 (1957).

[40] M. S. Kushwaha and S. S. Kushwaha, Phys. Status Solidi B **87**, 247 (1978).

[41] D. H. Dutton, B. N. Brockhouse, and A. P. Miiller, Can. J. Phys. **50**, 2915 (1972).

[42] G. Simmons and H. Wang, *Single Crystal Elastic Constants and Calculated Aggregate Properties: A Handbook*, 2nd ed. (MIT Press, Cambridge, MA, 1971).

[43] W. B. Pearson, *A Handbook of Lattice Spacing and Structures in Metals and Alloys* (Pergamon Press, Oxford, 1967), Vols. 1 and 2.

[44] C. J. Bradley and A. P. Cracknell, *The Mathematical Theory of Symmetry in Solids* (Oxford University Press, Oxford, 1972).

[45] D. D. Johnson, A. V. Smirnov, J. B. Staunton, F. J. Pinski, and W. A. Shelton, Phys. Rev. B **62**, R11917 (2000).

[46] The additional error may be attributed to the different magnetic states considered within the Connolly-Williams method (ferromagnetic) and KKR-CPA (paramagnetic).

[47] Durga Paudyal, Tanusri Saha-Dasgupta, and Abhijit Mookerjee, J. Phys.: Condens. Matter **16**, 7247 (2004).

[48] *Binary Alloy Phase Diagrams*, 2nd ed., edited by T. B. Massalski, H. Okamoto, P. K. Subramanion, and L. Kacprzak (American Society for Metals, Metals Park, OH, 1990).

[49] M. Hansen, *Constitution of Binary Alloys* (McGraw Hill, New York, 1958).

[50] Note that, in fact, the "spherical" nanoparticles used in the Monte Carlo simulation have a trancated-octahedron geometry (see Ref. 36).

[51] T. Tadaki, T. Kinoshita, Y. Nakata, T. Ohkubo, and Y. Hirotsu, Z. Phys. D: At., Mol. Clusters **40**, 493 (1997).

[52] L. D. Landau and E. M. Lifshitz, *Course of Theoretical Physics* (Pergamon, Oxford, 1980), Vol. 5.

[53] R. V. Chepulskii and W. H. Butler (unpublished).

[54] S. Kang, D. E. Nikles, and J. W. Harrell, Nano Lett. **2**, 1033 (2002).

[55] Z. W. Lu, S. H. Wei, A. Zunger, S. Frota-Pessoa, and L. G. Ferreira, Phys. Rev. B **44**, 512 (1991).